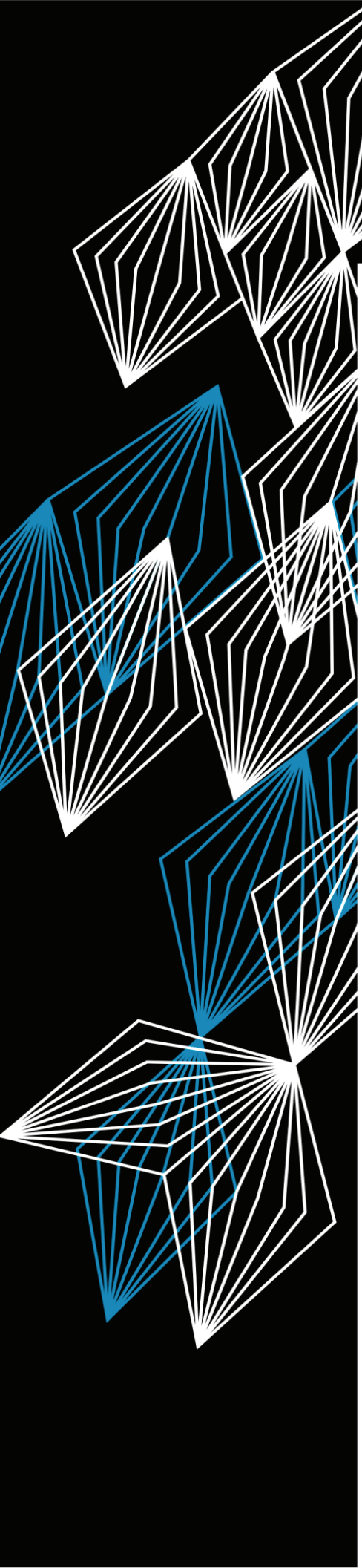

MASTER THESIS

A Modeling Framework for Magnetic Origami Devices using a Bar-and-Hinge Model

SAM TIJHUIS

FACULTY OF ENGINEERING TECHNOLOGY
DEPARTMENT OF BIOMECHANICAL ENGINEERING

EXAMINATION COMMITTEE
PROF. DR. S MISRA
DR. V. KALPATHY VENKITESWARAN
DR.IR. J.P. SCHILDER

UNIVERSITY OF TWENTE.

Thesis submitted by
Sam Tijhuis
under the supervision of
Prof. dr. S Misra,
Dr. V. Kalpathy Venkiteswaran, and
Dr.ir. J.P. Schilder
in order to fulfill the necessary requirements to obtain a Master's degree in
Mechanical Engineering at the University of Twente
and defended on
June 6, 2024

Abstract

Using the principles of origami folding, shape-changing structures and devices can be constructed. To control the shape-change of these devices magnetic actuation can be used. There are existing methods for simulating origami structures, but none of them incorporate magnetic actuation. This thesis presents a method for analyzing magnetically-actuated shape-changing origami devices. The modeling framework uses novel formulations to decompose a magnetic load to be compatible with a bar-and-hinge model. The formulations developed work for parallelogram and triangular panels, two panel shapes that are commonly used in origami structures. This allows for a large variety of origami structures to be simulated. An iteration algorithm is implemented to find an equilibrium between the magnetic torques of the magnets and the internal forces of the origami structure. A bar-and-hinge model is used to determine the deformation of a magnetic origami structure in a uniform magnetic field. The model is validated with multiple two-panel origami test samples and a six-panel waterbomb pattern sample. The samples are constructed from 3D-printed PLA panels connected with bendable thin steel hinges and neodymium magnets. The deformation of the test samples in a uniform magnetic field is compared to the simulations obtained from the magnetically actuated bar-and-hinge model. For the two-panel samples, the final deformation obtained from the model was within 4% of the experimental results. For the waterbomb pattern the difference was 8.5%. Two examples of origami patterns with a larger number of panels and hinges have been simulated. One example is a ten-panel Miura ori pattern made with parallelogram and rectangular panels. The other is a Huffman waterbomb pattern with seventeen panels that combines square and triangular panels. The model still has limitations, it only works for triangular and parallelogram panel shapes and in a static uniform magnetic field. Even with the limitations the modeling framework shows promising results and has opportunities for future expansion.

Table of Contents

List of Figures

List of Tables

1 Introduction

Minimally invasive techniques are being developed to make medical procedures as low-risk and safe as possible. The goal of minimally invasive surgery (MIS) is the reduction of trauma to the patient's body. This can be achieved by minimization or even elimination of surgical incisions [1]. As a result, the tools used for MIS need to be as small and compact as possible. Smaller surgical devices allow the surgeon to operate on parts of the body that are hard to reach and without causing significant physical trauma to the patient. The reduced physical trauma results in additional benefits for the patient: lower incidence of post-surgery complications, reduction of pain, quicker recovery, shorter length of hospital stay, minimal cosmetic disfiguration, decreased psychological impact, and overall improved quality of life [1]. A large challenge for devices and tools used in MIS is that the size of the device needs to be minimized without compromising its function.

One way to reduce the size of surgical devices is to make them foldable. Foldable devices are constructed in such a way that separate parts of the device can fold into each other, this can reduce the total space the device needs. When a device is folded into a smaller space it makes it easier for the device to be used in the human body without causing trauma to the body. A folded device can be transported to a specific location in the body and be unfolded to perform some function.

Folded devices like this can be created using techniques from the field of origami engineering, a type of engineering that uses origami to create engineering solutions. Conventionally origami uses paper that is folded by hand to create shapes with mainly artistic purposes. In origami engineering however the same principles that are used in paper folding are used in combination with engineering to create structures that fold like origami. This creates structures that can transform in ways that might not be possible with conventional engineering solutions. A reason to use origami in engineering is the shape-changing ability of origami structures. Similar to when a flat piece of paper is folded to create various different origami shapes, engineering origami can create structures that have multiple different shapes depending on how it is folded. Origami techniques have been used in aerospace engineering for deployable solar panels and sunshields [2]. Similar principles have been used to create stiff structures that could be used for deployable buildings or bridges [3]. Origami engineering also has medical applications such as devices used in tissue sealing [4] or tissue biopsy [5].

For most engineering solutions paper is not a suitable material so other materials are used, often these materials are a lot more rigid than paper which makes it hard to fold these materials. As a result, different solutions need to be used to create the foldability that is desired. This can be achieved by connecting rigid panels with flexible hinges. The flexibility of the hinge can be achieved by using a low-stiffness material [6,7], torsional hinges [8], or a mechanism such as a pin hinge. The hinges also need to account for the thickness of the panels of the structure [9].

A challenge with foldable origami is how to generate the folding movement. For medical applications this becomes more challenging since the scale is generally much smaller and electronic actuators are not always possible. One way to generate the folding movement is by magnetic actuation. With magnetic actuation, magnets are added to a device that can be controlled by applying magnetic fields that steer the magnets and actuate the device. These ideas have been used to create a soft robotic origami crawler as seen in Fig. 1b [6]. This Crawler consists of four magnetic hexagons plates that are connected with Kresling pattern origami tubes. The Kresling pattern is an origami shape that contracts when rotated. When a magnetic field is applied the plates rotate and the whole structure contracts. Repeating this motion allows the device to crawl. Magnetically controlled origami can also be used to create soft grippers that can be controlled wirelessly [7]. Such a device can be seen in Fig. 1a and uses magnetic panels connected by a soft substrate to construct a gripper. The model used to construct this device is based on the bar-and-hinge model developed by Liu & Filipov *et al.* and uses magnetic panels that have an in-plane magnetization [7,10].

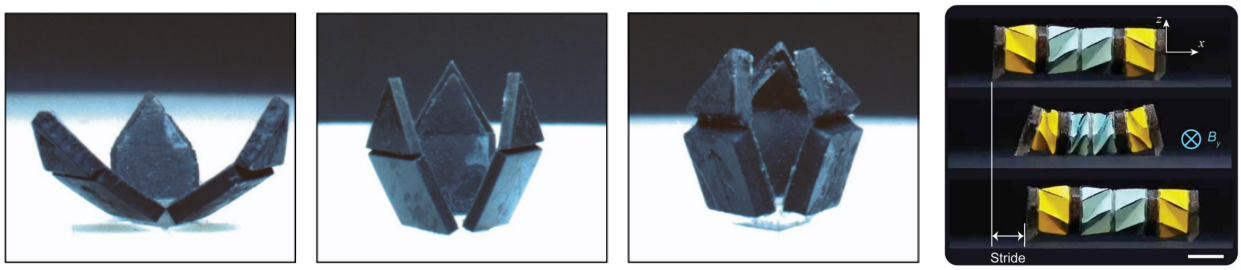

(a) (b)

Figure 1: (a) Soft robotic gripper at multiple stages during its activation [7]. (b) Origami soft robotic crawler showing the stride length achieved after magnetic activation [6]

For designing origami devices it would be useful to have a method that is capable of simulating magnetically controlled origami structures. The research done by Cui *et al.* [7] provides such a method by combining a bar-and-hinge model with magnetic actuation. The method used in this paper has one limitation however, it only works for in-plane magnetization. This means that the magnetic direction of each panel is always along the flat plane of each panel. For more complex origami shapes it might be useful to have the magnetic direction in any possible direction. The goal of this thesis is to expand the work done in previous research and create a simulation method that overcomes this limitation.

The research presented in this report uses a modified version of the bar-and-hinge model presented by Liu & Filipov *et al.* to approximate the mechanical behavior of 3D origami structures under a uniform magnetic field [10]. This model can simulate the deflection of an origami structure for any given crease pattern with predefined magnet placements and orientations.

The report is structured into five chapters. First, the theoretical background of origami and magnetic actuation are introduced. Then the bar-and-hinge model and a novel torque decomposition method needed for magnetic actuation are introduced. Next, the implementation of the new method in MATLAB is described. Multiple examples of origami patterns simulated using the model are shown as well as experiments to validate these results. Finally, the results are discussed.

2 Theoretical Background

2.1 Origami Engineering

Origami is the art of folding paper. In origami a flat piece of paper is transformed into any decorative or interesting shape, oftentimes representing an object or animal. Origami has primarily been associated with recreational and artistic uses. However, the materials and the uses of origami extend far beyond just paper and art [11]. The goal of origami is to transform a flat piece of material by only folding the material along straight crease lines. Two types of folds can be made: a valley and a mountain fold. Using the flat piece of material as a reference plane the crease line for a mountain fold moves up from the reference plane when folded and the valley fold moves down. This can be seen in Fig. 2. These folds can be combined to create a crease pattern, this crease pattern shows each fold and the type of fold that needs to be made to create the final shape. An example of the crease pattern of a paper airplane can be seen in Fig. 3. The crease pattern only shows what folds need to be made and where they are located but not the order in which the folds need to be made. In the airplane example the paper is rectangular in shape but for other origami patterns the outer edge of the paper could have any shape as long as the fold lines are straight.

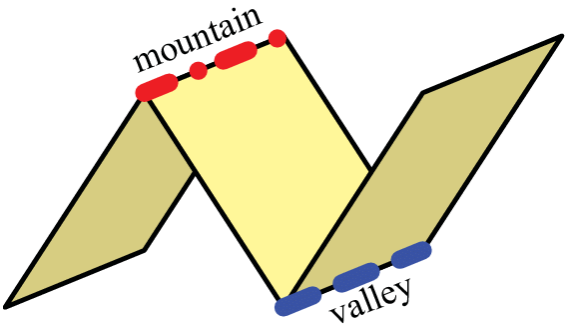

Figure 2: A fold in origami is either a mountain(left) or valley(right) fold. [12]

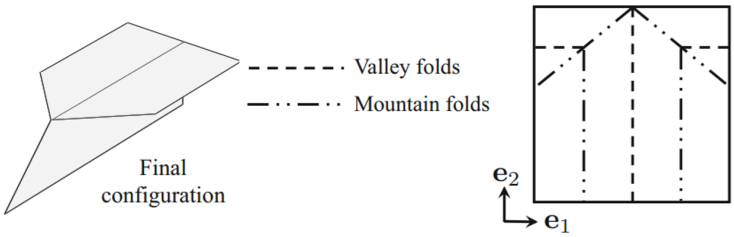

Figure 3: The crease pattern of a paper airplane [11]

In origami structures and crease patterns two regions can be identified: the folds and the faces. A face is the region that is bounded by the folds and the edges of the sheet. In Fig. 4 the folds and faces are indicated for a foldable cube and pyramid. In origami engineering the faces of the structure are generally made of rigid panels and the folds of a more bendable material, this ensures that the origami structure only folds along the fold lines and not the faces. For thin and easily foldable materials such as paper the folds occur along a single creased line with a small width. However for structures that have a larger thickness where directly creasing the materials is not possible or desired, folding can be obtained by bending a localized region as is also the case in Fig. 4. In the figure the folds are achieved by creating a thin rectangular strip between the faces that is made of an easily bendable material, this material is shown with a darker color in the figure.

The folding region can be designed in many different ways depending on the application of the origami structure. The construction and material of the fold mostly determine how the origami structure will deform when under load. To ensure the structure only folds along the fold lines the fold region always needs to have a lower stiffness than the panels. This can be achieved by using a material with lower stiffness for the fold

region so that the fold region will bend but the faces don't. One drawback of this fabrication method is that depending on the materials used the folds behave like springs that restrict the rotation of the faces. So generally materials with a low stiffness are the most suitable. The lower stiffness can also be achieved by strategically removing material in the fold region, this is called a strained joint [9]. Strained joints can also account for the thickness of the rigid panels allowing for the panels to be completely folded onto each other as can be seen in Fig. 5. Another option to create a fold is by using a mechanical hinge design such as a pin hinge. One advantage of this method is that these hinges don't have the spring behaviour that is present in other methods. A big drawback is that hinges are large then the other options and are thus mostly suitable for large scale origami mechanisms.

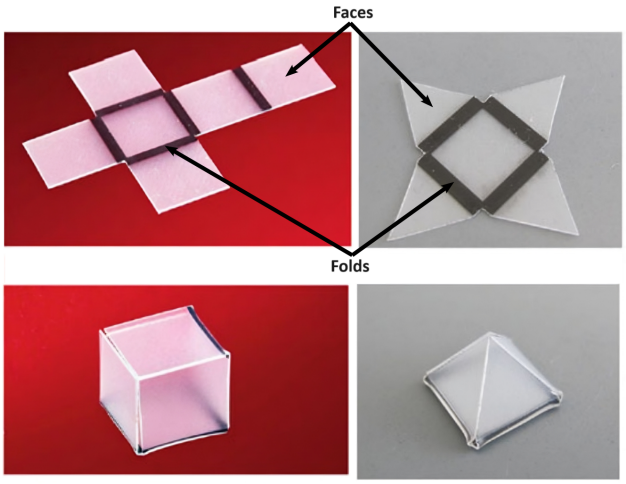

Figure 4: Identification of the faces and folds on a foldable cube(left) and pyramid(left) [11] [13]

Figure 5: Example of the bending of a strained joint in three stages [9]

2.2 Magnetic Actuation

To control the folding of the origami structures designed for this thesis magnetic actuation is used. An example of magnetic actuation of two origami panels can be seen in Fig. 6. The figure shows the magnetic directions of the panels, called the magnetic moment, with arrows inside the panels. An external uniform magnetic field is depicted as dotted lines. This creates a torque on the panels that makes the magnetic moment within the panels try to align with the applied magnetic field. This results in the magnetic moment and applied field pointing in the same direction.

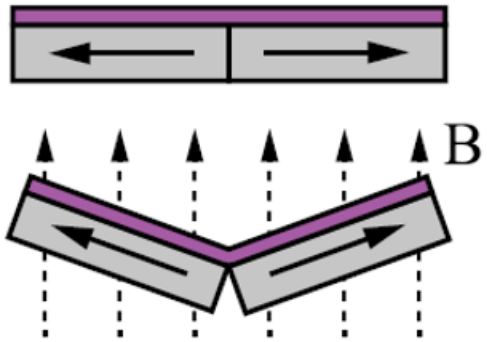

Figure 6: Two magnetic panels connected by a flexible hinge under uniform magnetic field [7]

Applying a magnetic field to a magnetic object results in forces and moments on the magnet. These forces($\boldsymbol{F}_m$) and moments($\boldsymbol{\tau}_m$) can be calculated as:

$$\boldsymbol{F}_m = \boldsymbol{m} \cdot \nabla \boldsymbol{B}, \tag{1}$$

$$\boldsymbol{\tau}_m = \boldsymbol{m} \times \boldsymbol{B}. \tag{2}$$

In the equation above $\boldsymbol{m}$ denotes the magnetic moment of the magnet and $\boldsymbol{B}$ the magnetic flux density. These formulas evaluate the magnet as a since point with a constant magnetic moment. The magnetic moment($\boldsymbol{m}$) of a magnet is a result of the size and type of magnet and can be calculated as:

$$\boldsymbol{m} = \frac{\boldsymbol{B}_r \boldsymbol{V}}{\boldsymbol{\mu}_o}. \tag{3}$$

In the equation above $\boldsymbol{V}$ denotes the volume of the magnet, $\boldsymbol{B}_r$ denotes the residual flux density and $\boldsymbol{\mu}_o$ is the vacuum magnetic permeability. $\boldsymbol{\mu}_o$ is constant and has a value of $4\pi \cdot 10^{-7}\text{N}\cdot\text{A}^{-2}$. $\boldsymbol{B}_r$ represents the magnetic induction remaining in a saturated magnetic material and shows how strong the magnet is. For neodymium magnets, the magnets used in this thesis, the $\boldsymbol{B}_r$ is related to its magnet grade generally being available between N35 and N55 with a higher value representing a higher strength [14]. These grades corresponds to $\boldsymbol{B}_r$ values of around 1.2 to 1.5 T.

The magnetic flux density density($\boldsymbol{B}$) in Eqns. 1 and 2 represents the strength and direction of the magnetic field that is applied to the permanent magnet. Changing this magnetic field allows for the control of the torques and forces on the permanent magnet. For the purposes of controlling magnetic origami the torque is the main factor of interest for this project. Applying a torque to panels allows for the rotation and alignment the panels in the required direction. Although applying a force on the magnetic panels could help with positioning the device, the analysis will be limited to only applying torques. For this reason a uniform magnetic field will be used. In a uniform magnetic field the magnetic flux density($\boldsymbol{B}$) is mostly constant over the volume of the field. This results in the gradient $\nabla \boldsymbol{B}$ being zero and the Force being zero. Another result of using a uniform magnetic field is that all panels within the magnetic field experience the same magnetic flux density. The torque from Eq. 2 will always be highest when the difference in angle between the magnetic moment and the applied magnetic field is the largest. As a result the torque will decrease when the angle between the magnetic moment and field is smaller.

2.2.1 Helmholtz coils

To generate a uniform magnetic field Helmholtz coils can be used. A Helmholtz coil is a device that can generate a nearly uniform magnetic field. This device consists of two identical circular electromagnets placed along a single axis. Both coils have the same eclectic current in the same direction. The experimental area is then located in between these two magnets and shown with a red dotted outline. An image of a pair of Helmholtz coils is shown in Fig. 7.

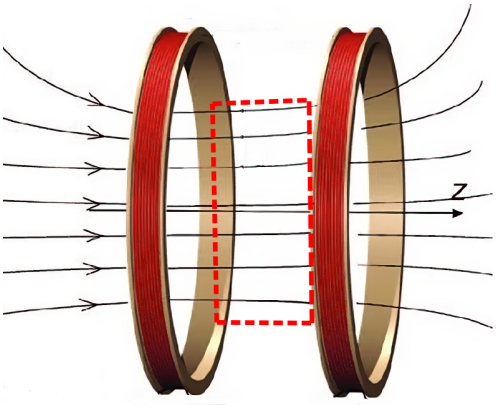

Figure 7: Two electromagnets that form a Helmholtz coil. Part of the magnetic field is indicated with arrows [14].

To minimize any non-uniformity between the two coils the optimal distance between the coils is the same as the diameter of both coils. From the centre of the coils along the Z-axis as indicated in Fig. 7 there is a 7% variation of field strength. The field strength along the Z-axis is shown in Fig. 8. The distance between the coils is indicated with d and the centre between the coils is at $z = 0$. For consistent results using Helmholtz coils the best results will be achieved when the magnetic device is as close to the centre as possible.

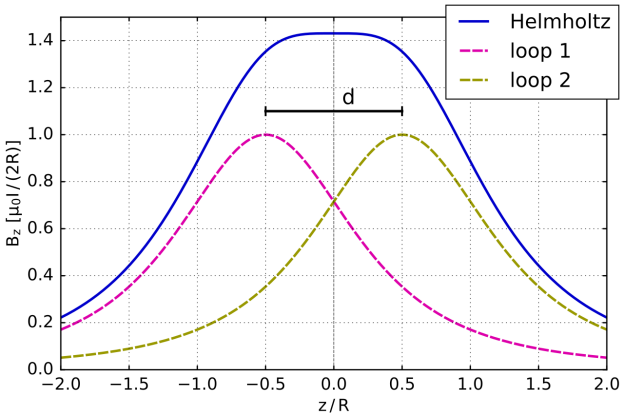

Figure 8: The magnetic field induction along the axis crossing the centres of both coils [15].

2.3 Analytical Tools for Origami Mechanics

To simulate the movement of an origami structure that is under some load, multiple approaches can be used. Generally these approaches can be divided into three categories: rigid-facet, lattice framework and finite element [16]. A rigid-facet approach assumes that the all the panels of the origami are rigid and the fold creases behave like hinges. The hinges can be defined as having a torsional stiffness and the origami is modeled as a planar linkage mechanism. This method is especially useful for modeling large tessellations

such as the Miura ori pattern since these can be simplified to a one degree of freedom system [17]. The lattice framework approach also referred to as the bar-and-hinge model uses bar elements to represent the fold lines and hinges to represent the torsional stiffness of the fold. This approach can also be used to model the deformation of the panels. This is done by including virtual bars across the panels that each have a bending hinge with a torsional stiffness [18]. This allows for simulating non-rigid origami as well as rigid origami. The lattice framework approach has more capabilities and a wider range of applications compared to the rigid-facet approach but is more complex in its application. The last approach is to model the origami with a finite element method. With this method a mesh can be created of the origami structure and the deformation for a specific load will be calculated. Some methods have also been developed where the panels are represented as shell elements and the fold lines as hinge joints similar to the rigid-facet and the lattice framework approach [16]. For this project a bar-and-hinge approach has been chosen because of its high efficiency. To validate the model while it is being adapted for magnetic actuation finite element simulations are done in COMSOL. The COMSOL simulations allows for a way to validate the bar-and-hinge model before doing physical testing.

3 Materials and Methods

In this chapter the mathematical methods used in the deflection simulation of origami is introduced. This includes the bar-and-hinge model and a torque distribution method that allows for torques to be applied to this model. The fabrication method and materials of the experimental origami are explained. Two different origami are simulated and tested in an experiment. Two more origami shapes are simulated as examples of how the program works.

3.1 Methods

3.1.1 Bar-and-hinge model

Any origami pattern can either be flat foldable or non-flat foldable. Flat foldable refers to whether it is possible to fold a crease pattern in such a way that when every crease is fully folded the whole folded sheet of paper lies flat. With non-flat folding this isn't possible. Any origami structure can also be developable or non-developable origami. Developable origami is origami that is folded starting from a flat piece of material. As previously described in section 2.3 a bar-and-hinge model will be used to calculate the deflection of origami structures under load. Specifically the method developed by Liu and Filipov *et al.* is used [18]. This method was chosen because it is able to simulate origami structures of any of the types mentioned above.

The bar-and-hinge model represents each quadrilateral face of the origami with 8 bars connected between 5 nodes. The bar elements can only stretch along its axis. This model is referred to as N5B8 and is shown in Fig. 9. The model uses material properties of the origami to determine the properties of the bars. These properties include the elastic modulus (E), the Poisson's Ratio (ν), the thickness of the panels (t) and the dimensions of the fold lines (w). Using these properties the stiffness of the bars can be calculated in such a way that it approximates the stretching of the origami face. For triangular panels only three nodes and three bars are used.

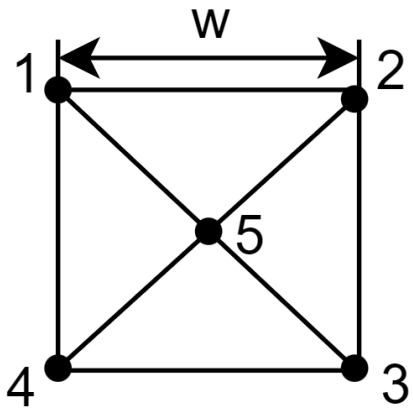

Figure 9: The N5B8 representation of an origami face.

There are three types of effects the model tries to capture: folding, bending and stretching. Folding represents the folding between the panels and occurs on the outer bars of the N5B8 model. Bending is the bending of the panel itself and occurs on the inner bars connected to node 5 in Fig. 9. Stretching of the panel is modeled by each bar being able to stretch along the length of the bar. The bending and the folding is modeled with virtual hinges that act as torsional springs. The springs can be seen in Fig. 10. Both hinges have specific stiffness values that are derived from the material and construction properties of the origami.

3.1.2 Nonlinear elastic formulation of the bar-and-hinge model

The origami structure is considered a nonlinear elastic system. With this method, the entire origami system will be modeled by using a global stiffness matrix $\boldsymbol{K}$. This stiffness matrix will relate the displacement of

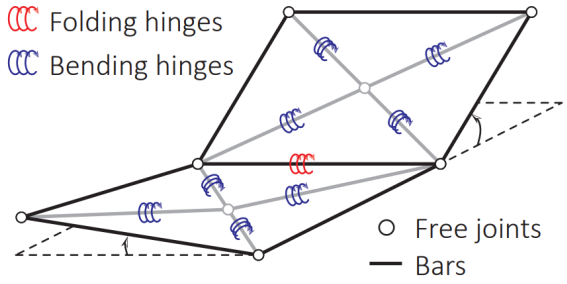

Figure 10: The bar-and-hinge model as described in [19].

each node $\boldsymbol{u}$ to the forces in the system $\boldsymbol{f}$. This is shown in:

$$\boldsymbol{K}\boldsymbol{u} = \boldsymbol{f}. \tag{4}$$

From Filipov and Liu it is obtained that the global stiffness matrix is constructed in the following way [18]:

$$\boldsymbol{K} = \begin{bmatrix} \boldsymbol{C} \\ \boldsymbol{J}_B \\ \boldsymbol{J}_F \end{bmatrix}^T \begin{bmatrix} \boldsymbol{D_S} & 0 & 0 \\ 0 & \boldsymbol{D_B} & 0 \\ 0 & 0 & \boldsymbol{D_F} \end{bmatrix} \begin{bmatrix} \boldsymbol{C} \\ \boldsymbol{J_B} \\ \boldsymbol{J_F} \end{bmatrix}. \tag{5}$$

In the above equation $\boldsymbol{C}$ is the compatibility matrix. This matrix relates the nodal displacements $\boldsymbol{u}$ to the bar extensions $\boldsymbol{e}$. $\boldsymbol{J_B}$ and $\boldsymbol{J_F}$ represent Jacobian matrices of bending and folding respectively. The Jacobian matrices relate the nodal displacements $\boldsymbol{u}$ to the change in angle $\boldsymbol{d\theta}$ which is different for bending and folding. For folding $\boldsymbol{d\theta_F}$ represents the angle between the panels. For bending $\boldsymbol{d\theta_B}$ represents the angle between two parts of the panel that are bending around one of the bending hinges. These relations can be represented as:

$$\begin{bmatrix} \boldsymbol{C} \\ \boldsymbol{J}_B \\ \boldsymbol{J}_F \end{bmatrix} \boldsymbol{u} = \begin{bmatrix} \boldsymbol{e} \\ \boldsymbol{d\theta_B} \\ \boldsymbol{d\theta_F} \end{bmatrix}. \tag{6}$$

The other parameters in Eqn. 5 represent various material stiffness properties. $\boldsymbol{D}_S$ incorporates stiffness parameters for the stretching and shearing of the panels. $\boldsymbol{D}_B$ includes the stiffness parameters for the bending of the panels. $\boldsymbol{D}_F$ has the stiffness parameters for the folding of the panels. Since every node has three degrees of freedom the global stiffness matrix $\boldsymbol{K}$ will have a size of 3N x 3N with N being the number of nodes. From Eqn. 5 three distinct contributions to the stiffness can be separated and written as:

$$\boldsymbol{K}(\boldsymbol{u}) = \boldsymbol{C}^{\boldsymbol{T}}\boldsymbol{D_S}\boldsymbol{C} + \boldsymbol{J}_{\boldsymbol{B}}^{\boldsymbol{T}}\boldsymbol{D_B}\boldsymbol{J_B} + \boldsymbol{J}_{\boldsymbol{F}}^{\boldsymbol{T}}\boldsymbol{D_F}\boldsymbol{J_F} = \boldsymbol{K_S}(\boldsymbol{u}) + \boldsymbol{K_B}(\boldsymbol{u}) + \boldsymbol{K_F}(\boldsymbol{u}). \tag{7}$$

The global stiffness matrix contains contributions from the bars $\boldsymbol{K_s}$, bending hinges $\boldsymbol{K_B}$ and folding hinges $\boldsymbol{K_F}$. The stiffness values all result from the material and construction properties of the origami structure. When using rigid panels with flexible hinges $\boldsymbol{K_S}(\boldsymbol{u})$ and $\boldsymbol{K_B}(\boldsymbol{u})$ will be significantly higher then $\boldsymbol{K_F}(\boldsymbol{u})$. $\boldsymbol{K_F}(\boldsymbol{u})$ is thus the main property used to design the mechanical behavior of origami structures with rigid panels.

To solve for the nodal displacements when a load is applied a total potential energy(Π) balance can be used. This energy balance contains contributions from the bar elements($\boldsymbol{U_S}$), the bending hinges($\boldsymbol{U_B}$) and the folding hinges($\boldsymbol{U_F}$) in a similar relation as the stiffness matrix of Eqn. 7. The total potential energy is written as:

$$\boldsymbol{\Pi}(\boldsymbol{u}) = \boldsymbol{U_S}(\boldsymbol{u}) + \boldsymbol{U_B}(\boldsymbol{u}) + \boldsymbol{U_F}(\boldsymbol{u}) - \boldsymbol{f}^{\boldsymbol{T}}\boldsymbol{u}. \tag{8}$$

In the above equation $\boldsymbol{f}$ is the applied nodal force. Using the principle of Stationary Potential Energy Filipov *et al.* [18] used the energy balance to construct the following force equilibrium equation :

$$\boldsymbol{T}(\boldsymbol{u}) = \boldsymbol{T_S}(\boldsymbol{u}) + \boldsymbol{T_B}(\boldsymbol{u}) + \boldsymbol{T_F}(\boldsymbol{u}) - \boldsymbol{f} = 0. \tag{9}$$

In the above equation $\boldsymbol{T_S(u)}$, $\boldsymbol{T_B(u)}$ and $\boldsymbol{T_F(u)}$ are internal forces and are nonlinear functions of $\boldsymbol{u}$.

To solve for the force equilibrium equation an arc-length solution scheme is used called the modified generalized displacement control method (MGDCM) [10]. This method introduces a new variable λ known as the load factor. This load factor controls the magnitude of the external loads following an incremental-iterative process. The following equilibrium equation shows how λ controls the external loads:

$$\boldsymbol{R}(\boldsymbol{u}, \lambda) = \boldsymbol{T(u)} - \boldsymbol{\lambda f} \tag{10}$$

In this equation $\boldsymbol{R}$ is the residual force. The idea of the MGDCM is to increase lambda over a set amount of increments. This means that for every increment only a part of the external load is applied. This results in the deflections slowly increasing for every increment. For every increment there also is an iterative process. With every iteration the residual in Eqn. 10 is minimized to within a specified error. The exact details of how the MGDCM is implemented can be found in Liu and Paulino [10]

3.1.3 Rotational spring elements

As described in the previous chapter two types of hinges are used in the model, a bending and folding hinge. In Fig. 10 each spring is placed on a bar that connects two triangular sections with each other. The two triangular sections are defined with 4 nodes forming two triangles as seen in Fig. 11. In the model the degree of rotation is the dihedral angle between the two surfaces of the triangles. The undeformed length of the hinge axis is denoted as L.

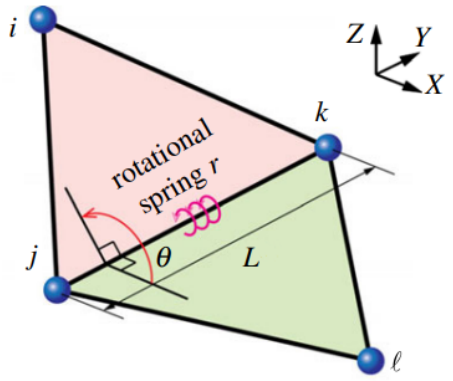

Figure 11: The components of a rotation spring element [10].

The rotational spring elements are defined using the global nodal coordinates without an intermediate step to local coordinates. It is assumed that the constitutive relationship for the rotational spring element can be described by a stored energy function $\psi = \psi(\theta)$, θ being the dihedral angle. The total stored energy of the rotational spring element is:

$$U_{spr} = \psi(\theta). \tag{11}$$

The spring element resists the rotation of the panels and generates a resistance moment defined by a partial derivative of the stored energy and the angle:

$$M = \frac{\partial \psi(\theta)}{\partial \theta}. \tag{12}$$

The internal force vector that results from this moment is defined as:

$$\boldsymbol{T}_{spr}(\boldsymbol{u}) = \tilde{\boldsymbol{T}}_{\boldsymbol{spr}} = \frac{d\psi}{d\theta}\frac{d\theta}{d\boldsymbol{x}} = M\frac{d\theta}{d\boldsymbol{x}}. \tag{13}$$

In the above equation $\boldsymbol{x}$ denotes the deformed nodal coordinates obtained from $\boldsymbol{x} = \boldsymbol{X} + \boldsymbol{u}$ where $\boldsymbol{X}$ are the undeformed nodal coordinates. Since $\boldsymbol{X}$ is constant the gradients with respect to $\boldsymbol{u}$ are equal to the gradient

with respect to $\boldsymbol{x}$. The tangent stiffness matrix is derived from the derivative of the internal force vector:

$$\boldsymbol{K}_{spr}(\boldsymbol{u}) = \tilde{\boldsymbol{K}}_{\boldsymbol{spr}} = k\frac{d\theta}{d\boldsymbol{x}} \otimes \frac{d\theta}{d\boldsymbol{x}} + M\frac{d^2\theta}{d(\boldsymbol{x})^2}. \tag{14}$$

In the previous equation $\otimes$ denotes the tensor product. The tangent rotational stiffness is denoted by k and equal to:

$$k = \frac{dM}{d\theta}. \tag{15}$$

3.1.4 Geometry of the rotational spring element

In the previous section the dihedral angle was used in the formulation of the tangent rotational stiffness. The angle is obtained from the four nodes (i, j, k, l) that define two triangles as seen in Fig. 12. The angle can be obtained from the nodes by defining two vectors based on the relations between them. A vector that connects two nodes is defined as:

$$\boldsymbol{r}_{qp} = \boldsymbol{x}_p - \boldsymbol{x}_q, \tag{16}$$

with p and q being the labels of any pair of nodes. Using the four nodes that define the triangles two vectors are created:

$$\boldsymbol{m} = \boldsymbol{r}_{ij} \times \boldsymbol{r}_{ij}, \tag{17}$$

$$\boldsymbol{n} = \boldsymbol{r}_{kj} \times \boldsymbol{r}_{kl}. \tag{18}$$

$\boldsymbol{m}$ and $\boldsymbol{n}$ are vectors that are normal to the two intersecting planes. Using these normal vectors the dihedral angle can be obtained by:

$$\theta = \arccos\left(\frac{\boldsymbol{m}\cdot\boldsymbol{n}}{\|\boldsymbol{m}\|\|\boldsymbol{n}\|}\right). \tag{19}$$

This does however not define the full rotation with the correct sign. To complete this definition a sign indicator η is added:

$$\theta = \eta \arccos\left(\frac{\boldsymbol{m}\cdot\boldsymbol{n}}{\|\boldsymbol{m}\|\|\boldsymbol{n}\|}\right) \bmod 2\pi, \tag{20}$$

with η defined as:

$$\eta = \begin{cases} sgn(\boldsymbol{m}\cdot\boldsymbol{r}_{kl}), & \boldsymbol{m}\cdot\boldsymbol{r}_{kl} \neq 0 \\ 1, & \boldsymbol{m}\cdot\boldsymbol{r}_{kl} = 0. \end{cases} \tag{21}$$

In the above equations, mod refers to the modulo operator which returns the remainder when divided by 2π. For $\boldsymbol{r}_{kl} = 0$ a value for η of 1 is used, this exception occurs when the angle is either 0 or π meaning that both panels lie in the same plane.

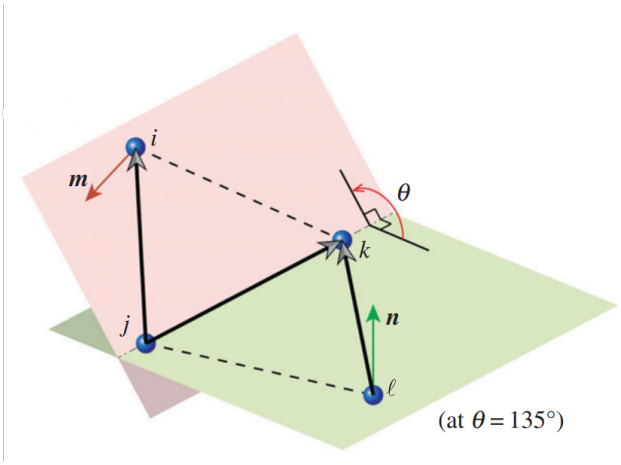

Figure 12: The geometry of a rotational spring element with the angle between two intersecting planes denoted with two colours [10].

3.2 Force distribution

The bar-and-hinge model is capable of calculating deflections as a result of forces applied to nodes in the structure. The magnetic actuation introduced in section 2.2 is able to generate torques as a result of an applied magnetic field. Since the bar-and-hinge model uses force as its input a method to change the torque load into a force load is needed. Methods for this have have been developed before [7], however there are limitations to how the magnet can be oriented. For this reason a more general method to apply magnetic actuation using a bar-and-hinge model was developed. The goal of this method is to obtain forces that result in the same deflection as applying a torque does. Two force decomposition methods were constructed; one for parallelogram panels and one for triangular panels. With these panel shapes a large variety of origami patterns can be constructed.

3.2.1 Parallelogram shaped panel

A force distribution method for parallelogram panels was developed, the steps of the decomposition are shown with a square panel. This is done because the concept is more easily explained with a square panel, but the resulting formulations also apply to parallelogram panels. A square panel is shown in Fig. 13 with the applied torque shown in red. The applied torque needs to be decomposed into four equivalent nodal forces. This is done in two steps. First, the applied torque ($\boldsymbol{\tau}$) is decomposed into four torques ($\boldsymbol{\tau}_1, \boldsymbol{\tau}_2, \boldsymbol{\tau}_3, \boldsymbol{\tau}_4$) that are applied to each bar of the panel. Second, the decomposed torques are used to obtain the nodal forces. The four decomposed torques are all normal to one of the bars, this is necessary for the second step where the nodal forces are constructed.

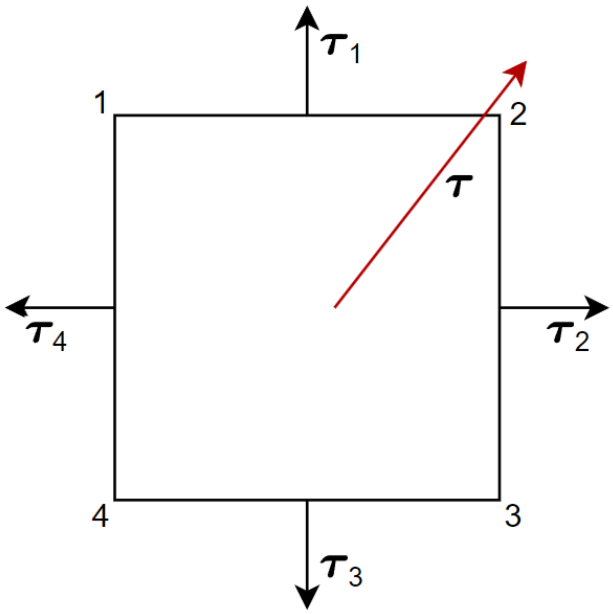

Figure 13: A square panel with an applied load shown in red and four torques on the bars shown in black.

The torques on the bars should add up to the applied torque, this results in:

$$\boldsymbol{\tau} = \boldsymbol{\tau}_1 + \boldsymbol{\tau}_2 + \boldsymbol{\tau}_3 + \boldsymbol{\tau}_4. \tag{22}$$

Using the geometry of the panels the outward normal vector $\boldsymbol{n}$ can be constructed for each of the four bars. These normal vectors are in the same direction as the decomposed torques. To solve for the values of the four torques four new variables are introduced: a_1, a_2, a_3 and a_4. These new variables are scalars that together with the normal vector represent the torques. Using these variables the previous equation can be written as:

$$\boldsymbol{\tau} = a_1\boldsymbol{n}_1 + a_2\boldsymbol{n}_2 + a_3\boldsymbol{n}_3 + a_4\boldsymbol{n}_4. \tag{23}$$

One constraint that can be used to simplify this equation is that the torques should be equally divided over the four bars. For a rectangular panel shape this results in $\boldsymbol{\tau_1} = \boldsymbol{\tau_3}$ and $\boldsymbol{\tau_2} = \boldsymbol{\tau_4}$. This simplification also works for panels shaped like a parallelogram since the bars opposite from each other are also the same size and orientation. The previous equation now simplifies to:

$$\boldsymbol{\tau} = 2a_1\boldsymbol{n_1} + 2a_2\boldsymbol{n_2}. \tag{24}$$

If the panel surface is chosen as the xy-plane the normal vectors only have x and y components n_x and n_y. The two equations for the applied torque in x and y directions can be used to solve a_1 and a_2:

$$\tau_x = 2a_1 n_{1x} + 2a_2 n_{2x}, \tag{25}$$

$$\tau_y = 2a_1 n_{1y} + 2a_2 n_{2y}. \tag{26}$$

Using substitution and solving for a_1 and a_2 results in:

$$a_1 = \frac{\tau_y n_{2x} - n_{2y}\tau_x}{2n_{1y}n_{2x} - 2n_{1x}n_{2y}}, \tag{27}$$

$$a_2 = \frac{\tau_y n_{1x} - n_{1y}\tau_x}{2n_{2y}n_{1x} - 2n_{1y}n_{2x}}. \tag{28}$$

With the solution for a1 and a2 the x and y components of the decomposed torques can be found. The z component can be found by equally dividing the applied torque along the four bars. For calculating the forces on the nodes the torques need to be perpendicular to the bars, the reason for this will be shown in the next step where the nodal forces are derived. By having the z component of the torque be equally divided the torques are still perpendicular to the bars. The final formulas for the decomposed torques are:

$$\boldsymbol{\tau_1} = \boldsymbol{\tau_3} = \begin{bmatrix} a_1 n_{1x} \\ a_1 n_{1y} \\ \frac{\tau_z}{4} \end{bmatrix}, \tag{29}$$

$$\boldsymbol{\tau_2} = \boldsymbol{\tau_4} = \begin{bmatrix} a_2 n_{2x} \\ a_2 n_{2y} \\ \frac{\tau_z}{4} \end{bmatrix}. \tag{30}$$

As can be seen in Fig. 13 every bar has a torque applied that is perpendicular to the bar. The free body diagram of bar element 1 is shown in Fig. 14. Using the decomposed torque, forces can be found at the end points of the bars that represent the applied torque. The forces shown in the figure are part of the total force on a node.

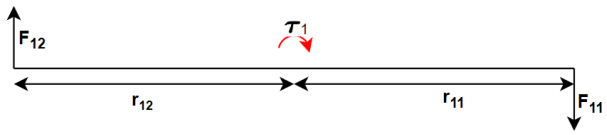

Figure 14: Bar element with a torque $\boldsymbol{\tau}_1$ that results in two forces $\boldsymbol{F}_{11}, \boldsymbol{F}_{12}$.

To find the forces on the bars a new parameter is introduced: $\boldsymbol{r_{ik}}$. $\boldsymbol{r_{ik}}$ is the length vector that goes from the center of bar i to the end point in node k. i is the bar index ($i = 1, 2, 3, 4$) and k the index of the node ($k = 1, 2, 3, 4$). A cross product between the torque and the length vectors gives the correct direction of the forces. This cross product is then divided by the length of $\boldsymbol{r_{ik}}$, which is obtained using a dot product. Each node is connected to two bars and each bar has a torque on it that creates a nodal force. This means that each node has force contributions from two bars that are summed together. The nodal forces for each node are:

$$\boldsymbol{F}_k = \sum_{i=k-1}^{k} \frac{1}{2} \frac{\boldsymbol{\tau}_i \times \boldsymbol{r}_{ik}}{\boldsymbol{r}_{ik} \cdot \boldsymbol{r}_{ik}}. \tag{31}$$

In the above equation index i is cyclic meaning that the index can only be $i = 1, 2, 3, 4$ and increasing the index when $i = 4$ gives $i = 1$. This is used for node $k = 1$, the index becomes $i = k - 1 = 4$. Node 1 is connected to bars 1 and 4 thus the force has contributions from those bars. The equation uses the node and bar numbering from Fig. 13.

3.2.2 Triangular panel

For a triangular panel the approach is similar to that of the square panel. The first step is to create three outward normal torques that should add up to the applied torque. This can be seen in Fig. 15.

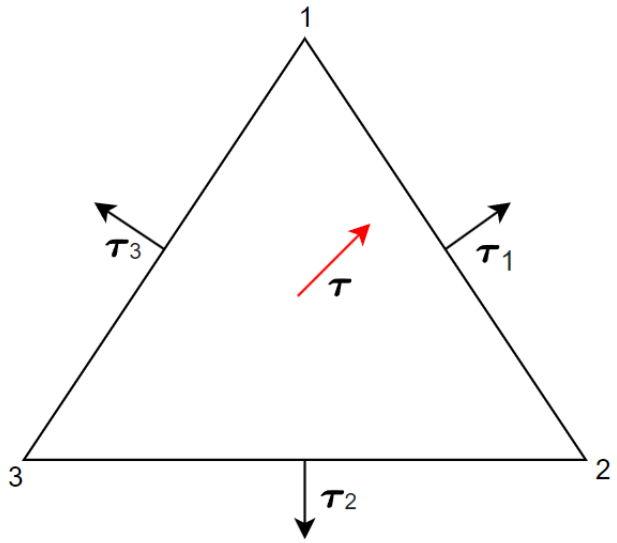

Figure 15: A triangular panel with an applied torque shown in red and three decomposed torques shown in black

The applied torque is divided into three torques that consist of the parameters a_1, a_2 and a_3 together with the three normal vectors $\boldsymbol{n_1}$, $\boldsymbol{n_2}$ and $\boldsymbol{n_3}$. The torque decomposition is shown as:

$$\boldsymbol{\tau} = a_1\boldsymbol{n_1} + a_2\boldsymbol{n_2} + a_3\boldsymbol{n_3}. \tag{32}$$

If the panel is chosen as the xy-plane two equations for the x and y components of the torque can be made in the same way as was done in Eqns. 25 and 26:

$$\tau_x = a_1 n_{1x} + a_2 n_{2x} + a_3 n_{3x}, \tag{33}$$

$$\tau_y = a_1 n_{1y} + a_2 n_{2y} + a_3 n_{3y}. \tag{34}$$

Without adding more constraints this cannot be solved. However, to obtain nodal forces that approximate the applied torque only two decomposed torques are necessary with the third one being zero. This is because for a triangle any selection of two bars is always connected to all three nodes. This allows for three nodal forces to be obtained that still approximate the applied torque. Since the torques are always normal to the bars and their direction cannot be altered there is a preference as to which torques are chosen to be decomposed and which torque is chosen to be zero. To obtain nodal forces that are evenly distributed across the three nodes it is best to choose the torques without a zero component in x or y direction. For example in Fig 15 $\boldsymbol{\tau_2}$ is in the negative y direction having no x component. $\boldsymbol{\tau_2}$ cannot apply any torque in the x direction leading to an uneven distribution of the forces across the nodes. An edge case is possible where two bars are at 90deg to each other and in the x and y directions. In this case the torque is simply distributed between the two perpendicular bars since both can only apply torque in one direction. One bar has the x component of the applied load and the other bar the y component. For the example triangle given in Fig. 15 the solutions to a_1 and a_3 are:

$$a_1 = \frac{\tau_x n_{3y} - n_{3x}\tau_y}{n_{1x}n_{3y} - n_{3x}n_{1y}}, \tag{35}$$

$$a_3 = \frac{\tau_x n_{1y} - n_{1x}\tau_y}{n_{3x}n_{1y} - n_{1x}n_{3y}}. \tag{36}$$

For this example $\boldsymbol{\tau_2}$ is chosen to be zero and the equations for the other torques are given as:

$$\boldsymbol{\tau_1} = \begin{bmatrix} a_1 n_{1x} \\ a_1 n_{1y} \\ \frac{\tau_z}{3} \end{bmatrix}, \tag{37}$$

$$\boldsymbol{\tau_3} = \begin{bmatrix} a_3 n_{3x} \\ a_3 n_{3y} \\ \frac{\tau_z}{3} \end{bmatrix}. \tag{38}$$

For different orientations and shapes of a triangular panel a different torque might be chosen to be zero giving similar equations for a_1, a_2 and a_3. Obtaining the nodal forces is done in the same way as in Eqn. 31.

3.2.3 Force distribution validation

The force distribution method described in the previous paragraphs changes an applied torque into multiple forces that approximate the torque. The distributed forces should result in the same deformation. To validate if an applied torque is kinematically equivalent to the distributed forces the deformation of a two panel origami is analysed using FEA. The origami can be seen in Fig. 16 and consists of two panels connected with a hinge with a specified bending stiffness. The darker panel is fixed with the other panel able to rotate around the hinge axis. One way to obtain the rotation of the panel under a specified load is by using $\boldsymbol{\tau} = \boldsymbol{K\theta}$. With $\boldsymbol{\tau}$ being the applied torque, $\boldsymbol{K}$ the bending stiffness and $\boldsymbol{\theta}$ the angle. This method can be compared to the bar-and-hinge model described in the previous paragraphs. The bar-and-hinge model uses the distributed forces according to Eqn. 31 as the input. A finite element simulation is also performed using COMSOL which can be seen if Fig. 17. With COMSOL both torques and forces can be applied to the two panel system and compared directly.

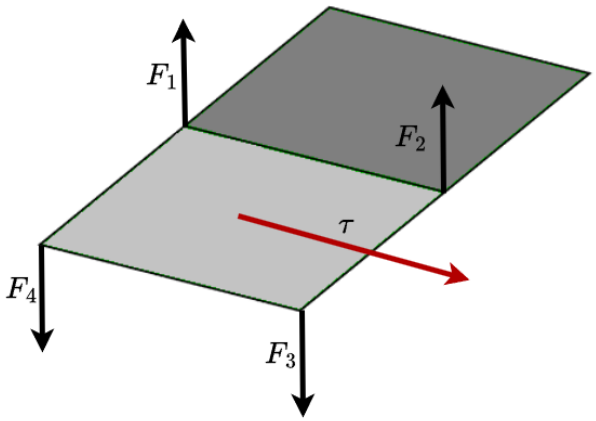

Figure 16: Two panels connected by a hinge with the axis of rotation of the applied torque shown in red and the resulting distributed forces shown in black.

The two panels used in the simulations are square with a size of 25mm by 25mm. The hinge is made of a thin steel sheet with dimensions: h=0.05mm, b=25mm and L=2.5mm. These dimensions are similar to those used in later testing. To calculate the bending stiffness $K = EI/L$ is used with $I = bh^3/12$. The properties for the simulations are given in table 1.

Table 1: Table containing the inputs needed to calculate the deflection.

Property	Value
E	$200 \cdot 10^9$ GPa
I	$2.6 \cdot 10^{-4}$ mm^4
K	0.0208 Nm/rad
ν	0.3

The torque and forces are shown in Fig. 16 and are equal to:

$$\boldsymbol{\tau} = \begin{bmatrix} 0.015 \\ 0 \\ 0 \end{bmatrix} Nm, \tag{39}$$

$$\boldsymbol{F_1} = \boldsymbol{F_2} = \begin{bmatrix} 0 \\ 0 \\ 0.3 \end{bmatrix} N, \tag{40}$$

$$\boldsymbol{F_3} = \boldsymbol{F_4} = \begin{bmatrix} 0 \\ 0 \\ -0.3 \end{bmatrix} N. \tag{41}$$

The resulting angles for four different methods are shown in table 2. The goal of these tests is to compare a torque load to a distributed force load. Two COMSOL results are compared against each other and the hand calculation is compared to the bar-and-hinge model. The hand calculation using $\boldsymbol{\tau} = \boldsymbol{K\theta}$ is very close to the bar-and-hinge model with the distributed forces. The small difference can be caused by the bending and stretching of the panels since the hand calculation assumes the panels to be rigid and the bar-and-hinge model doesn't. In COMSOL two different ways of applying a load were used. One panel is defined as a rigid connector, this makes the panel itself rigid and allows for a torque to be applied to the surface of the panel. The other method in COMSOL uses the distributed forces and applies them as point loads in each corner of the panel the same as in Fig. 16. The point loads are also defined such that they are always normal to the panel. Both methods in COMSOL gave the same deformation. From these results, it can be concluded that the force distribution method for square panels can be used to obtain forces that are kinematically equivalent to the applied torque.

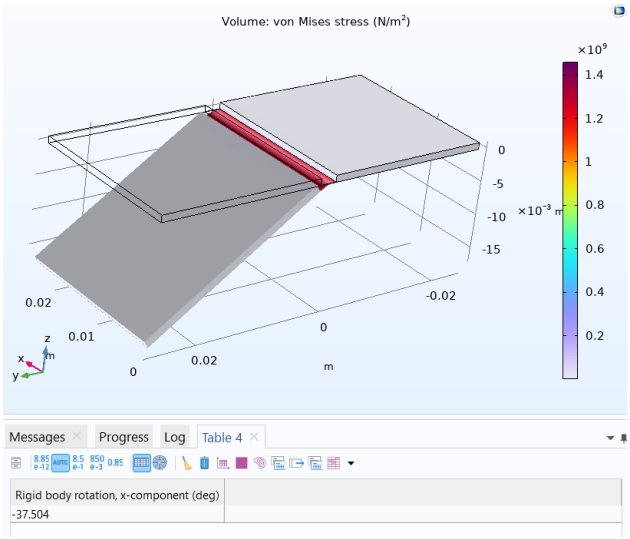

Figure 17: COMSOL deformation results using four point loads.

Table 2: Table containing the results for four different methods for calculating the deflection of the two panel origami.

Method	Input load	Angle
Hand calculation	Torque	41.25°
bar-and-hinge	Distributed forces	41.33°
COMSOL rigid connector	Torque	37.50°
COMSOL point loads	Distributed forces	37.50°

3.3 Implementation of the magnetic actuation

In the previous chapter formulations for magnetic actuation and torque distribution were described. To implement these formulations the MERLIN program developed by Liu *et al.* [19] is adapted to include magnetic actuation. MERLIN is a MATLAB program that uses the bar-and-hinge model described in section 3.1.1 to calculate the deflection of an origami structure based on an applied load. Similar to how the deflections are calculated an incremental iterative process is used. An iterative process is implemented to account for the change in magnetic moment direction as the panels rotate. While the incremental process applies the magnetic field in smaller increments. In the iterative process the magnetic moment is defined for the initial configuration and the deflection is calculated using the starting magnetic moment. As the structure deflects and the panels rotate the magnet orientation changes and as a result the magnetic torque is different from the initial configuration. For the next iteration the deflection is calculated again using the new orientation of the magnets. To update the magnetic moment a rotation matrix that relates the initial magnetic moment to the magnetic moment of the current iteration is created.

$$\boldsymbol{M}_{iter} = \boldsymbol{R}_M \boldsymbol{M}_0. \tag{42}$$

In the above equation $\boldsymbol{R}_M$ is the rotation matrix that is used to calculate the new orientation of the magnets($\boldsymbol{M}_{iter}$) by rotating the initial position($\boldsymbol{M}_0$). Both $\boldsymbol{M}_{iter}$ and $\boldsymbol{M}_0$ are unit vector only containing the direction of the magnets and are scaled with the strength of the magnet when the torque is calculated using Eqn. 2. $\boldsymbol{R}_M$ is calculated from the nodal positions in the deformed and undeformed state. To construct this rotation matrix two axis systems are created: one in the initial configuration($\boldsymbol{R}_0$) and another in the deformed configuration($\boldsymbol{R}_w$). These axis systems can be seen as the local coordinate systems for each panel. Both axis system are constructed in the following way.

$$\boldsymbol{R} = \begin{bmatrix} \boldsymbol{r}_{12} & \boldsymbol{n} & \boldsymbol{r}_{12} \times \boldsymbol{n} \end{bmatrix}. \tag{43}$$

In the above equation $\boldsymbol{r}_{12}$ is the length vector that connects the first two nodes of a panel according to Eqn. 16 and $\boldsymbol{n}$ is the normal vector and points outward from the panel. The third column is the cross product of $\boldsymbol{r}_{12}$ and $\boldsymbol{n}$ which creates a three axis system with all axis perpendicular to each other. The rotation matrix that shows the rotation between both axis systems is constructed as:

$$\boldsymbol{R}_M = \boldsymbol{R}_w \boldsymbol{R}_0^{-1}. \tag{44}$$

Since each magnet always point in the same direction in relation to the local coordinate system of the panel the magnet is located on the rotation of the magnetic moment directions is the same as that of the rotation of the local coordinate system of each panel.

Using the rotation matrix to update the magnetic moment results in a different torque according to Eqn. 2. This results in new deflections with a new position of the magnets. This process is then repeated until the change of magnetic moment between iterations is below a certain tolerance. This results in the behaviour seen in Fig. 18, where the rotation of three iterations are shown for a two panel system. The forces on the system are the same as shown in Fig 16. The first iteration will always overshoot the final position since the torque is highest when the difference between $\boldsymbol{M}$ and $\boldsymbol{B}_a$ is greatest. The second iteration undershoots while the third iteration is within the tolerance and is the final position.

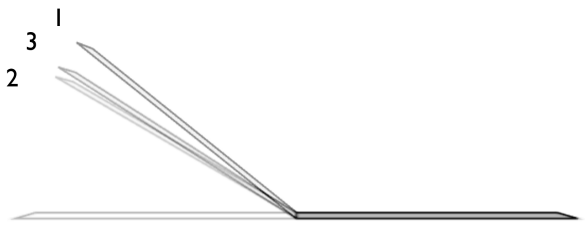

Figure 18: Undamped behaviour of the iteration process on a two panel origami.

To limit this over and undershoot the change in magnetic moment is damped. This is done by limiting the amount the magnetic moment can change from the previous iteration. Damping also improves the amount of iterations necessary to satisfy the tolerance requirement. Another method used to improve the robustness and the amount of iterations is by applying the magnetic field in smaller increments. The applied magnetic field is scaled by an increment value(inc) which increases for each increment, in the example below the field is scaled in 10 equal steps. This also allows for observations on how the origami moves as the magnetic field is changing. To speed up the computation a lower tolerance(tol_i) can be used for the incremental steps with the final tolerance(tol) being used for the last increment. This does result in the deformation being less accurate for the incremental steps so both tolerances need to be adjusted depending on what information is relevant to the specific simulation. An overview of how the incremental iterative process is applied can be seen in the algorithm below.

Iteration algorithm

---

define $damp$,tol and tol_i ▷ Values are adjusted for different origami patterns

for incr = 0.1 : 0.1 : 1 ▷ Set the amount and size of the increments, final incr is always 1

  iter=1,$\boldsymbol{B}_{ai}$ = incr ·$\boldsymbol{B}a$ ▷ $\boldsymbol{B}_a$ is scaled by the increment value

  if incr = 1

    $tol_i = tol$ ▷ A smaller tolerance is used to calculate the final increment

  end if

  while $res > tol_i$ ▷ The while loop keeps updating until the residual is smaller than tol_i

    $\boldsymbol{\tau} = \boldsymbol{M}_{iter-1} \times \boldsymbol{B}_{ai}$ or $\boldsymbol{\tau} = \boldsymbol{M}_0 \times \boldsymbol{B}_{ai}$ ▷ First iteration uses $\boldsymbol{M}_0$

    $\boldsymbol{\tau} \rightarrow \boldsymbol{F}$ ▷ The torque is converted to forces using the torque decomposition

    $\boldsymbol{F} \rightarrow \boldsymbol{u} \rightarrow \boldsymbol{M}_{iter}$ ▷ The MERLIN program finds the deflections which updates $\boldsymbol{M}_{iter}$

    $\boldsymbol{M}_{iter} = \boldsymbol{M}_{iter-1} + \frac{\boldsymbol{M}_{iter} - \boldsymbol{M}_{iter-1}}{damp}$ ▷ Damping is applied to $\boldsymbol{M}_{iter}$

    iter = iter+1

    res = $norm(\boldsymbol{M}_{iter} - \boldsymbol{M}_{iter-1})$ ▷ The residual is obtained from the change in $\boldsymbol{M}_{iter}$

  end while

end for

---

4 Results

4.1 Test setup

To validate the simulation method a test setup is needed. As described in section 2.2.1 Helmholtz coils are used to apply a uniform magnetic field. Three coils are combined in order to apply a uniform magnetic field in any direction. The test setup can be seen in Fig. 19 with the experiment area outlined in red. The coils have different sizes so they can all apply a field in the same area. The samples are placed in the experiment area using aluminum t-slot profiles.

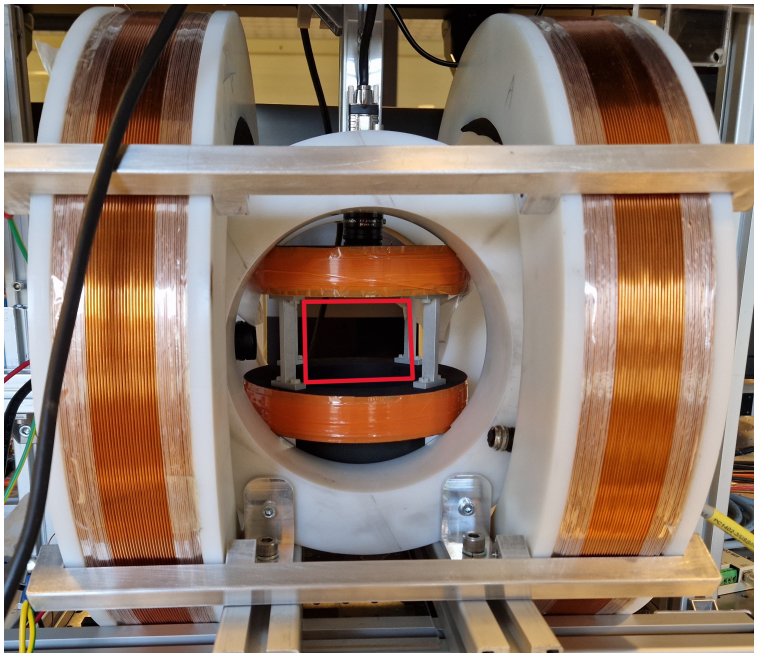

Figure 19: Test setup of the three-axis helmholtz coil with the experiment area outlined in red.

4.2 Two-panel origami

To validate the magnetically actuated bar-and-hinge model the deformation of a two-panel origami is simulated using MATLAB script described in section 3.3 and compared to experimental data.

4.2.1 Two-panel origami problem setup

The pattern that was used for the two-panel origami can be seen in Fig. 20a. Each panel and each node is numbered with the nodes that define panel 1 being fixed and nodes 1 and 3 free to move.

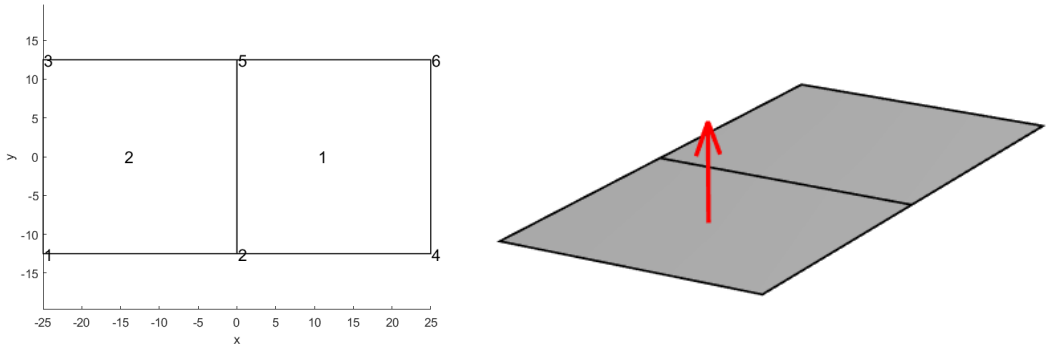

(a) (b)

Figure 20: (a) Two-panel origami pattern with the node and panel numbers. (b) Two-panel origami with red arrows to indicate the magnetic moment direction of the initial configuration.

The magnetic moment is defined as a matrix with every column of the magnetic moment matrix being equal to the magnetic moment of a panel. Since panel 1 is fixed only panel 2 has a nonzero magnetic moment:

$$M = \begin{bmatrix} 0 & 0 \\ 0 & 0 \\ 0 & 0.112 \end{bmatrix} \text{Am}^2. \tag{45}$$

The magnets used are N48 neodymium discs with a diameter of 8mm and a thickness of 1mm. Each magnet has a magnetic moment of 0.056 Am^2 and two are placed on panel 2. The magnetic moment can be seen in Fig. 20b.

A magnetic field of 40mT is applied in the negative x direction. This results in the following torque for the initial configuration:

$$\boldsymbol{\tau} = \begin{bmatrix} 0 & 0 \\ 0 & -4.48 \\ 0 & 0 \end{bmatrix} \text{Nmm}. \tag{46}$$

$\boldsymbol{\tau}$ is defined as a matrix with each column equal to the torque of a panel. This torque is obtained in the undeflected state. As the algorithm iterates and the panel folds, the torque will decrease since the magnet orientation changes to align with the field.

4.2.2 Two-panel origami MATLAB simulation

The origami pattern can be manually defined however for larger origami patterns this can become time consuming. The MERLIN program also allows for .obj files to be used as the input for the origami pattern. This file contains all the dimensions and fold information needed for the simulation. To generate this file Freeform origami is used [20]. Freeform origami is an origami simulation tool that is used to generate .obj files from .dxf files. The .dxf file contains a 2D drawing of the origami pattern and is made in CAD software. The standard settings of Freeform origami are used with the planar facets setting turned on. The planar facets setting ensures that only the faces defined in the drawing are included in the .obj file.

The first step in the simulation is to change the applied torque to a force load. The force matrix is defined with the node numbers in the first column and the other columns containing the XYZ components of the force on that node. The torque from Eq. 46 is decomposed which results in:

$$\boldsymbol{F} = \begin{bmatrix} 1 & 0 & 0 & -89.60 \\ 2 & 0 & 0 & 89.60 \\ 3 & 0 & 0 & -89.60 \\ 4 & 0 & 0 & 0 \\ 5 & 0 & 0 & 89.60 \\ 6 & 0 & 0 & 0 \end{bmatrix} \cdot 10^{-3}\text{N}. \tag{47}$$

A summary of the variables used in the simulation are shown in table 3. The stiffness in the table is the stiffness per unit length. Multiple sizes of this origami pattern were tested so the total hinge stiffness is K_f times the width of the hinge. The increment step was set to be 0.0250 so that with every step $\boldsymbol{B}_a$ is increased with 1 mT. The tolerance on the residual is dependent on the amount of panels. For a small amount of panels, a small tolerance can be used to obtain good accuracy, with more panels a higher tolerance is used since the residual is larger.

Table 3: Variables used in the two-panel origami

$\boldsymbol{B}_a$(mT)	K_f(Nm/rad)	Damping	Increment step	Residual tolerance
$\begin{bmatrix} -40 \\ 0 \\ 0 \end{bmatrix}$	0.1960	2	0.0250	0.005

The final deflected configuration of a 25mm square panel can be seen in Fig 21. The results of these simulations are used in the next section to compare against experimental data.

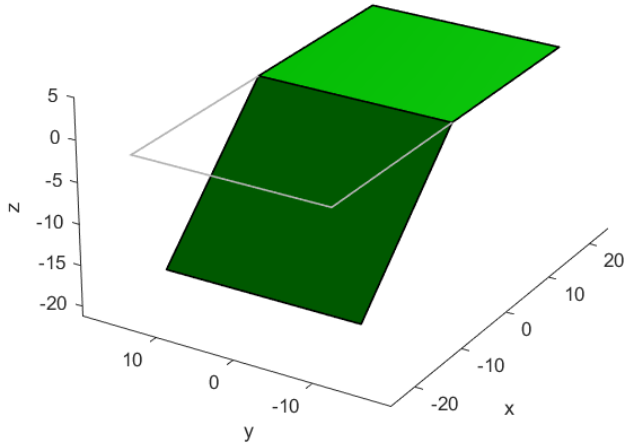

Figure 21: The final configuration of a two-panel origami under an applied magnetic field.

4.2.3 Helmholtz experiment sample

The goal of this experiment is to compare the bend angle obtained from the simulation to the results from the test setup. A sample was made with the same dimensions used in the simulation of section 4.2.1. The exact dimensions of the origami sample can be seen in Fig. 22a. The tolerance of the hinge thickness is included according to the specification of the manufacturer [21]. Three different values for the width (w) where tested: 20, 22.5 and 25mm. By varying the width, the hinge stiffness for each sample is different. The round cutout in the center of each panel is where a magnet is placed. One of the samples can be seen in Fig. 22b. The samples are constructed from cold-rolled C100S carbon steel sandwiched between 3D-printed PLA. The sandwich is created by applying double-sided tape to the 3D printed panels and placing this in a mold that holds the panels in the correct position according to the drawing in Fig. 22a. The steel sheet is cut to the correct dimensions and pressed down onto the tape while the panels are fixed in the mold. The process is repeated for the other side to create a symmetric structure. Finally, one magnet is placed on each side of the steel sheet. Both magnets are placed to have their magnetic moment aligned in the same direction.

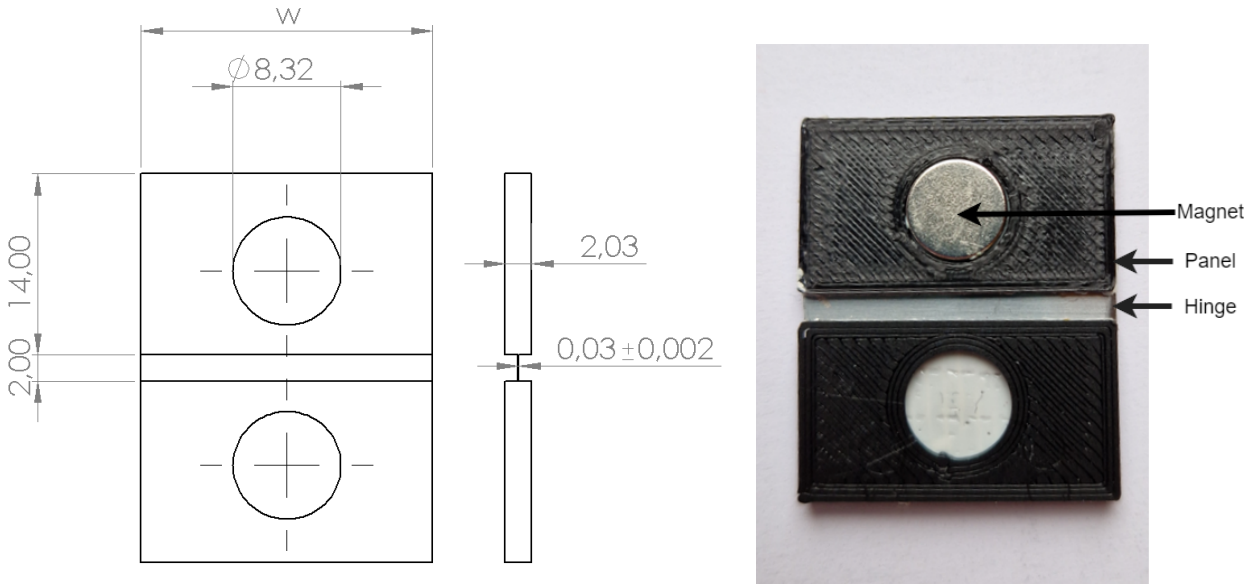

(a) (b)

Figure 22: (a) Dimensions of the test samples in mm with the width (w) being varied for each sample. (b) Test sample with the magnet placed at the center of the top panel.

4.2.4 Helmholtz experiment setup

All three samples were tested in a uniform magnetic field generated with a Helmholtz coil as described in section 2.2.1. One panel is fixed while the magnetic panel can bend along the hinge. The table below shows the magnetic moment (M) using Eqn. 3 and the stiffness (K) computed using EI/L for all three samples. To account for any possible fabrication errors, the stiffness is calculated by measuring the width and panel gap from the samples. The thickness of the hinge is harder to accurately measure over the width (w) of the sample. For this reason the tolerance of $\pm 2 \cdot 10^{-3}$mm is included since this can have a large effect on the bending stiffness.

Table 4: Table containing the properties of test samples

Width(mm)	K(Nmm/rad)	M(Am^2)
20	4.3±0.8	0.112
22.5	4.6±0.9	0.112
25	4.8±0.9	0.112

The samples are placed in the test setup described in section 4.1. One panel is fixed and the sample is oriented on its side so that gravity does not affect the bending of the hinge. A magnetic field is then applied in 40 steps of 1mT. An image is taken of each step generating 40 images. The test setup shows the sample when no field is applied in Fig. 23a. The sample when 40mT is applied can be seen in Fig. 23b. The applied field and magnetic moment of the magnet are also shown in the figures.

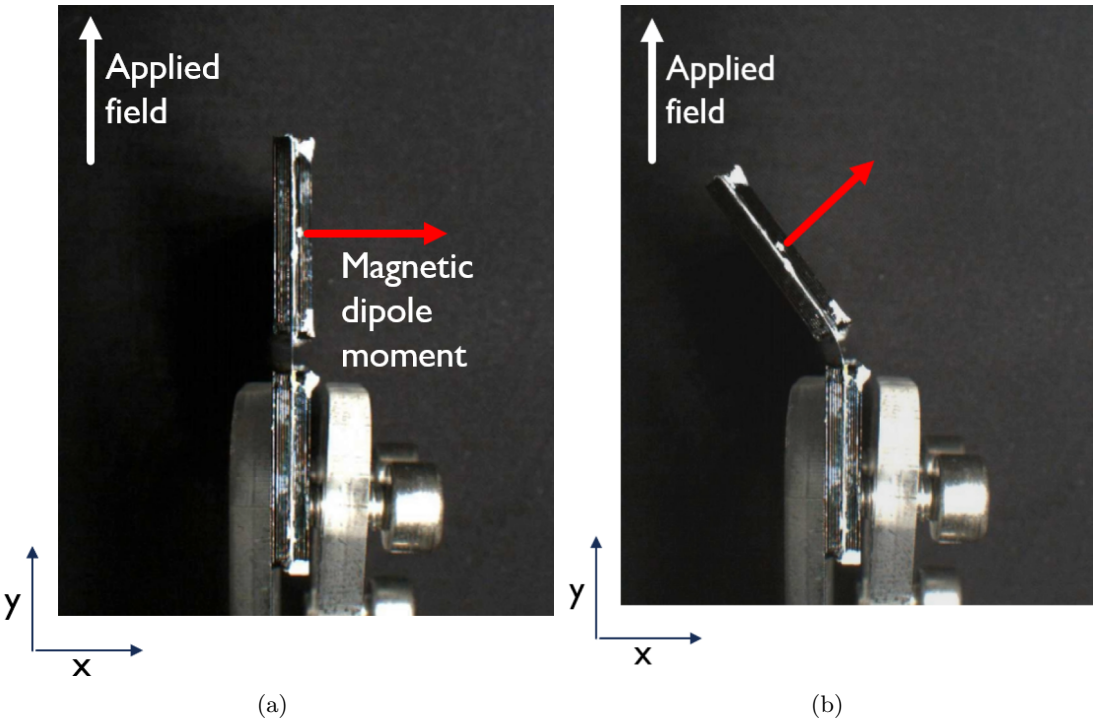

(a) (b)

Figure 23: (a) The test sample from a top view while the applied field is zero. (b) Test sample in a 40mT uniform magnetic field pointing in the y direction.

Using the white dots on the side of the samples and a motion tracking software called Kinovea the images are analyzed to find the coordinates of the panels [22]. Using the motion tracking data the bend angle for each image was calculated.

4.2.5 Helmholtz experiment results

In Fig. 24a the change in angle for increasing magnetic field is shown for all three samples. The dotted lines show the results obtained from the simulation and the other lines show the experimental results. The figure shows that the experimental results have larger deflections than the simulation results. For all samples, the difference between the experiment and the simulation is largest in the middle of the graph around 20mT. The final angle obtained from the model is on average within 4% of the experimental results.

To show how the stiffness can affect the results Fig. 24b shows the angle plot for the 25mm wide panel using the upper and lower limit of the stiffness tolerance that results from the thickness tolerance in Fig. 22a.

The black line shows the angle plot for the nominal stiffness while the grey area shows the possible deviation. The experimental results are included in blue.

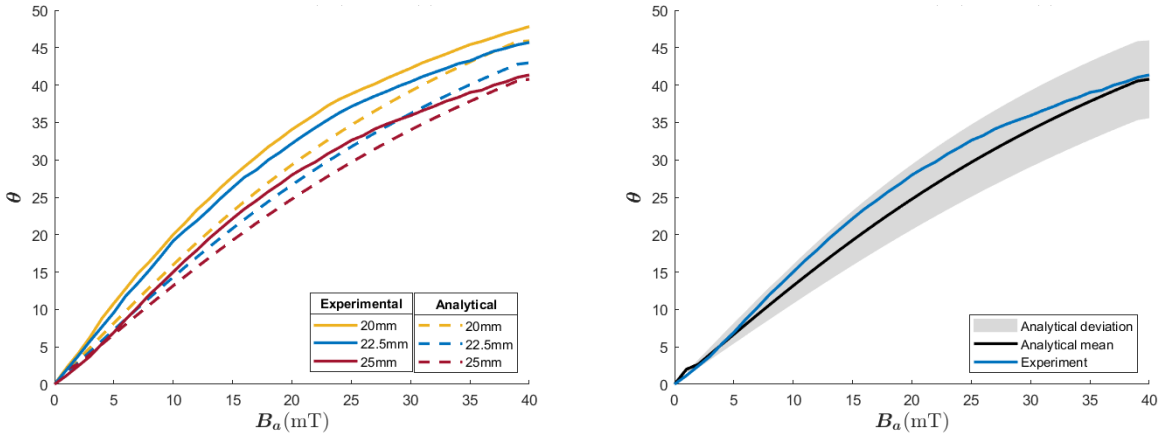

(a) (b)

Figure 24: (a) The applied field vs the angle for all three samples including the simulated angle. (b) The applied field vs the angle of the 25mm sample including the upper and lower limit that results from the stiffness tolerance.

The stiffness of the hinge is one of the most important parameters used in the simulation. Using the angle of the panel the stiffness of the samples can be calculated as the panel is deforming. The change in stiffness of the experimental results can be seen in Fig. 25. At lower B_a the stiffness has a large variance, this is likely due to measurement error since the deflection at this field strength is very small making it harder to measure accurately. The stiffness increases as the field increases, the cause of this increase is not clear. The stiffness value is calculated from the angle of the panel and the torque of the magnet. The torque of the magnet is not measured however and is calculated based on the position of the magnet which is assumed to be the same as that of the panel. This calculation also assumes that the fixed panel is oriented in the same direction as the applied field. In Fig. 23a the bottom panel should be perfectly vertical in the y-direction, however, the orientation is done manually and could lead to errors.

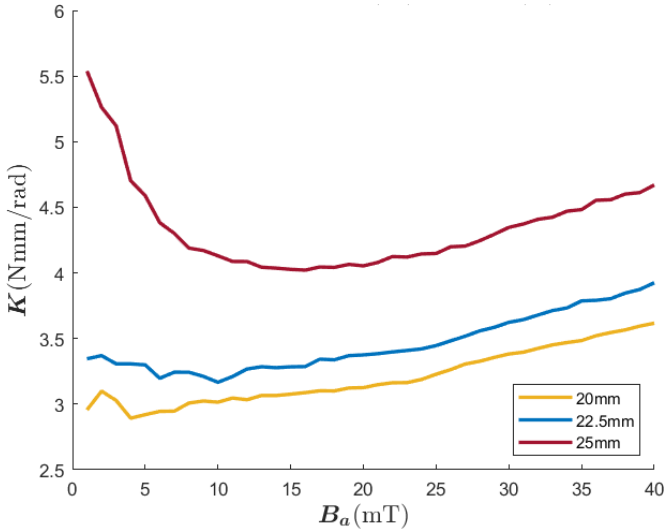

Figure 25: The stiffness for increasing field strength of three samples with a different hinge width.

4.3 Example 1: Waterbomb

To test a more complicated origami pattern a waterbomb origami was designed. This origami pattern folds similarly to an umbrella and uses a combination of mountain and valley folds. This pattern can fold flat, meaning that if all fold lines are folded completely the resulting structure would be flat. To test this origami the pattern is designed and simulated using the adapted MERLIN program. Then, a sample is constructed and examined in a uniform magnetic field.

4.3.1 MATLAB simulation

As for the previous tests the design is drawn in CAD and exported as a .dxf file. This is then converted to an .obj file using Freeform origami [20]. The node and panel numbers used in the simulation are shown in Fig. 26a. The nodes connected to panel 1 are all fixed with all other nodes free.

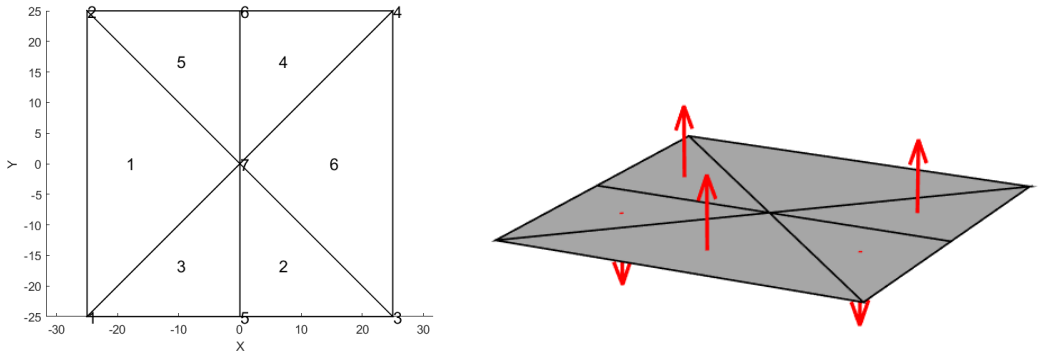

(a) (b)

Figure 26: (a) Waterbomb origami pattern with the node and panel numbers. (b) Waterbomb origami pattern with red arrows to indicate the magnetic moment direction of the initial configuration.

The magnetic moment is defined for each panel and can be seen in Fig. 26b where the direction is shown with red arrows. Since this pattern has six panels the magnetic moment matrix has six columns one for each panel:

$$\boldsymbol{M} = \begin{bmatrix} 0 & 0 & 0 & 0 & 0 & 0 \\ 0 & 0 & 0 & 0 & 0 & 0 \\ 0 & -0.112 & 0.112 & -0.112 & 0.112 & 0.224 \end{bmatrix} \text{Am}^2. \tag{48}$$

Panel 1 is fixed and has no magnets, panels 2 to 5 have 2 magnets and panel 6 has 4 magnets. Each magnet has a magnetic moment of 0.056 Am^2.

A magnetic field of 40 mT is applied in the positive x direction which results in the following torque and forces matrices:

$$\boldsymbol{\tau} = \begin{bmatrix} 0 & 0 & 0 & 0 & 0 & 0 \\ 0 & -4.48 & 4.48 & -4.48 & 4.48 & 8.96 \\ 0 & 0 & 0 & 0 & 0 & 0 \end{bmatrix} \text{Nmm}, \tag{49}$$

$$\boldsymbol{F} = \begin{bmatrix} 1 & 0 & 0 & 0.18 \\ 2 & 0 & 0 & 0.18 \\ 3 & 0 & 0 & 0 \\ 4 & 0 & 0 & 0 \\ 5 & 0 & 0 & -0.36 \\ 6 & 0 & 0 & -0.36 \\ 7 & 0 & 0 & 0.36 \end{bmatrix} \text{N}. \tag{50}$$

In the initial flat configuration the only torque generated is around the y axis. The force matrix is defined with the node numbers in the first column and the other columns containing the xyz components of the force. The torque for the initial configuration results in only forces in the z direction.

A summary of the other variables used in the algorithm described in section 3.3 are shown in table 5. The stiffness in the table is the stiffness per unit length and is multiplied by the length of the hinge to obtain the bending stiffness of a specific hinge. This value is used since not all hinges are the same length. A damping value of 4 was used since it resulted in a small number of iterations for this origami pattern. The increment step was set to be 0.0250 so that with every step $\boldsymbol{B}_a$ is increased with 1mT.

Table 5: Variables used in the waterbomb simulation

$\boldsymbol{B}_a$(mT)	K_f(Nm/rad)	Damping	increment step	residual tolerance
$\begin{bmatrix} 40 \\ 0 \\ 0 \end{bmatrix}$	0.1960	4	0.0250	0.1

The deflection as a result of the applied magnetic field can be seen in Fig. 27a. The side view can be seen in Fig. 30. Two panel edges are highlighted in red, the angle between these two panels is used for validation in the next section.

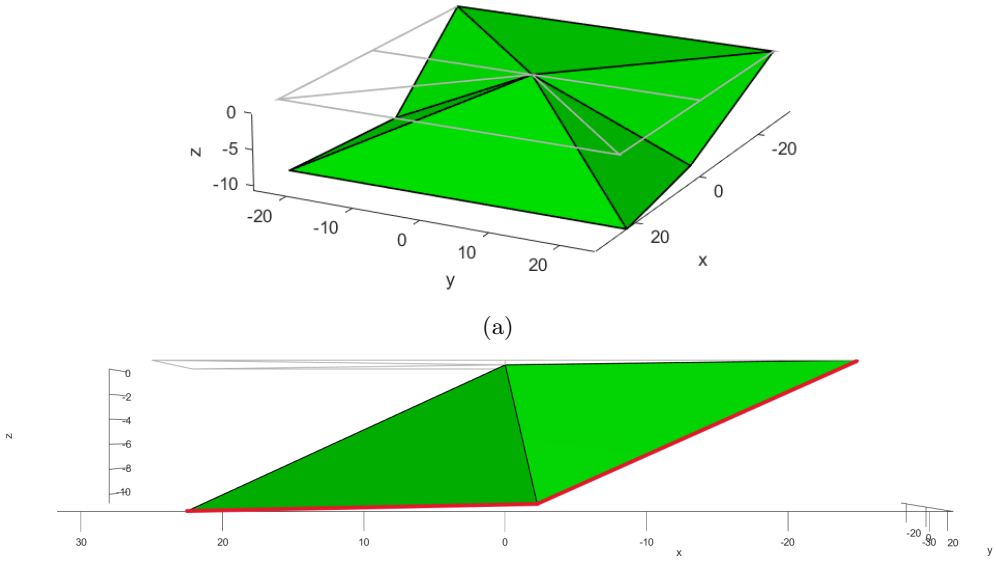

(a)

(b)

Figure 27: (a) The final configuration of the waterbomb origami. (b) Side view of the final configuration with two panel edges highlighted in red.

4.3.2 Helmholtz experiment

The same fabrication techniques as described in section 4.2.3 were used to construct the waterbomb pattern. The only difference is that a hole was created in the center of the origami. This is done to make each hinge a rectangle of which the stiffness is known. This also ensures that the hinges are connected to only the panels and not to each other. The waterbomb sample can be seen in Fig. 28. The colors are used to distinguish the panels from each other.

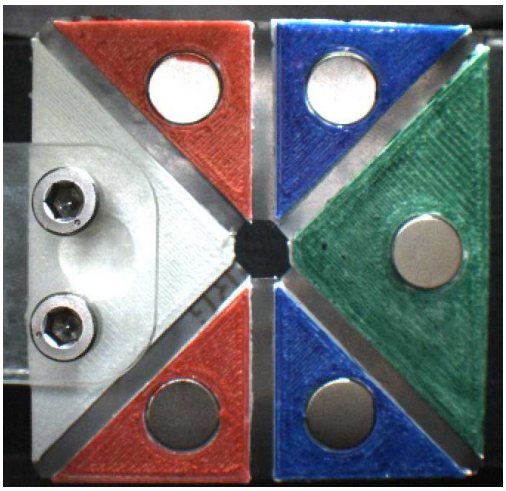

Figure 28: The waterbomb sample in the experimental setup.

The sample is placed in the test setup on its side to minimize the effect of gravity on the hinges. The top view can be seen in Fig. 30. The applied magnetic field is applied in positive x direction. The top of the figure shows the sample at 0mT and the bottom at 40mT. The magnetic moment direction of the blue and red panels are shown with red arrows.

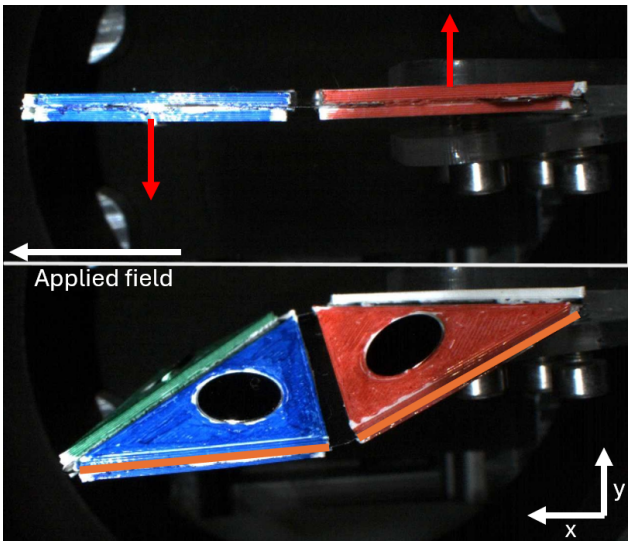

Figure 29: The waterbomb sample in the experimental setup at 0mT and 40mT.

In Fig. 30 two orange lines are drawn on the edges of the red and blue panels, the angle between these lines is used to compare the experiment to the simulation data. A plot of the applied field vs the angle is shown in Fig. 30. The black line is the analytical data and the blue line is the experimental. Similar to the two-panel tests the experimental data has a larger curvature compared to the more straight line of the

analytical data. The difference between the final angle of the analytical model and the experimental results is 8.5%

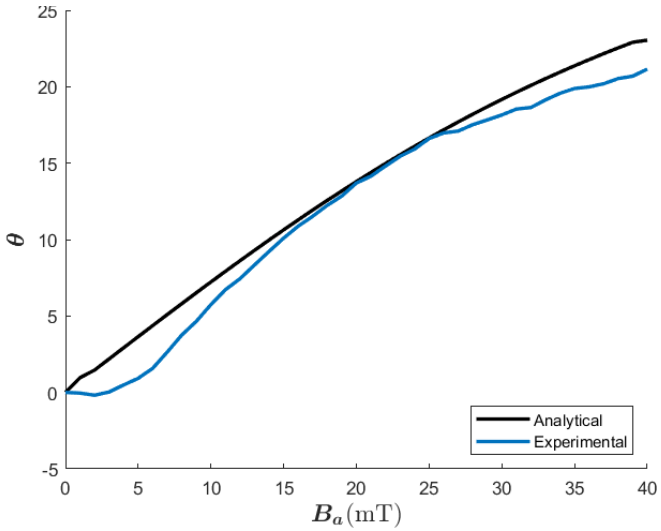

Figure 30: Plot of the magnetic field vs the angle. The angle between the two highlighted panels in Fig. 30 is shown in blue. The results from the MATLAB simulation are shown in black.

4.4 Example 2: 10 panel Miura ori

A common origami pattern is the Miura Ori, which is a combination of parallelograms that are mirrored to create a symmetric shape. The pattern can be repeated to create a tessellation that is flat folding. For this example, 8 panels of the Miura Ori are tested. The pattern can be seen in Fig. 31a. The pattern also includes two extra panels labeled 9 and 10 in the figure, panel 9 is used as the fixed panel and panel 10 is used to make it symmetric. The extra panels are added to allow the other panels to move freely without having to be fixed since one of the panels needs to be fixed for the simulation.

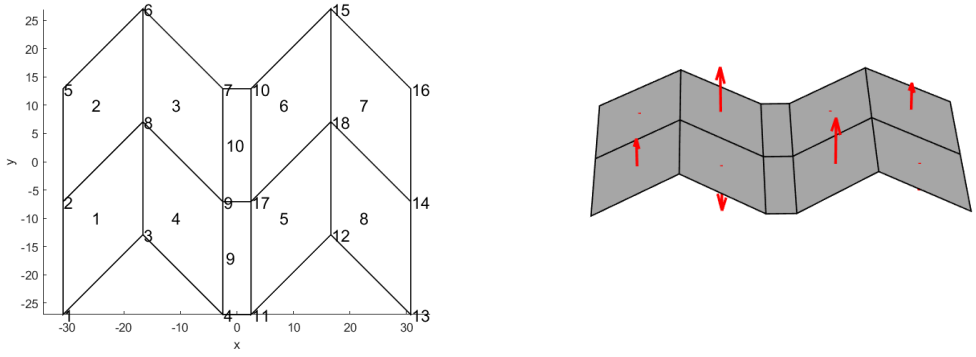

(a) (b)

Figure 31: (a) Miura Ori origami pattern with the node and panel numbers. (b) Miura Ori origami pattern with red arrows to indicate the magnetic moment direction of the initial configuration.

A magnetic moment is defined for each panel. The directions of the magnetic moment are placed in such a way that if the origami is fully folded the magnetic moment would align with the direction of the magnetic field. For this example all magnetic moments would point towards the positive x direction. Since this pattern has 10 panels the magnetic moment matrix has 10 columns one for each panel:

$$\boldsymbol{M} = \begin{bmatrix} 0 & 0 & 0 & 0 & 0 & 0 & 0 & 0 & 0 & 0 \\ 0 & 0 & 0 & 0 & 0 & 0 & 0 & 0 & 0 & 0 \\ 0.15 & -0.15 & 0.25 & -0.25 & 0.25 & -0.25 & 0.15 & -0.15 & 0 & 0 \end{bmatrix} \text{Am}^2. \tag{51}$$

For this pattern, it was found that panels 3 to 6 needed higher magnetic moments to obtain the desired deformation. These panels correspond to the middle four panels of the Miura Ori and are connected to other panels on both sides. This likely makes it require higher moments to actuate compared to the outer panels which are less restricted in their movement.

A magnetic field of 40 mT is applied in the positive x direction which results in the following torque matrix in the initial configuration:

$$\boldsymbol{\tau} = \begin{bmatrix} 0 & 0 & 0 & 0 & 0 & 0 & 0 & 0 & 0 & 0 \\ 6 & -6 & 10 & -10 & 10 & -10 & 6 & -6 & 0 & 0 \\ 0 & 0 & 0 & 0 & 0 & 0 & 0 & 0 & 0 & 0 \end{bmatrix} \text{Nmm}. \tag{52}$$

The example is set up similarly to the waterbomb pattern so in the initial flat configuration the only torque generated is around the y axis. As a result the forces obtained from the force decomposition are all in the z direction. A summary of the variables used in the algorithm are shown below in table 6. The stiffness and damping are the same as for the previous tests. The increment step is 0.25, this divides the applied field into 4 smaller increments. As a result $\boldsymbol{B}_a$ increases by 10mT for each increment. Since for this example the deflection does not have to be accurate for each increment but only for the final increment an intermediate tolerance is used as described in the algorithm of section 3.3. The final increment has a smaller tolerance of 0.1.

Table 6: Variables used in the Miura Ori simulation

$\boldsymbol{B}_a$(mT)	K_f(Nm/rad)	Damping	increment step	residual tolerance	intermediate tolerance
$\begin{bmatrix} 40 \\ 0 \\ 0 \end{bmatrix}$	0.1960	4	0.25	0.1	0.5

The final deflection that is obtained is shown in Fig. 32. The structure has the desired folding behavior of the Miura ori pattern where lower panels 1,4,5 and 8 have valley folds and upper panels 2,3,6 and 7 have mountain folds. A rotation of about 35° is obtained for the upper panels and a deflection of 14mm at nodes 6 and 14.

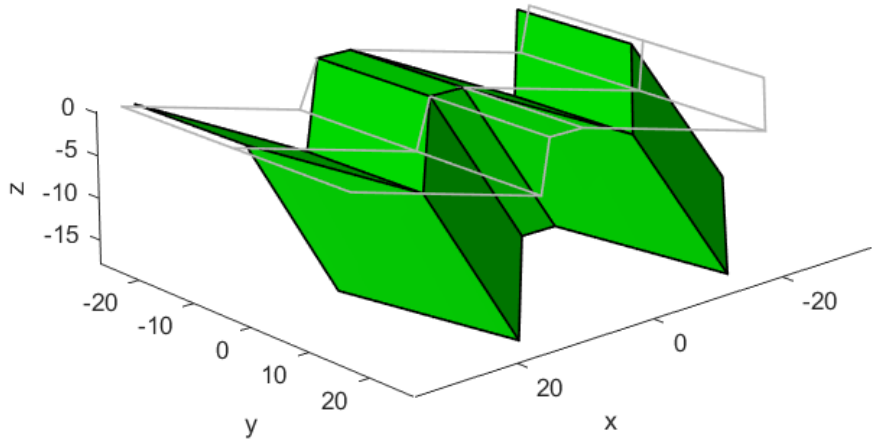

Figure 32: The final configuration of a Miura Ori origami under an applied magnetic field.

4.5 Example 3: Huffman waterbomb

Another example of an origami pattern that can be used as part of a larger tessellation is the Huffman waterbomb. The design with node and panel numbers is shown in Fig. 33a. This pattern has a square panel in the center with triangular panels around it. The triangle panels are all shaped so that they combine to form squares of the same size as the center square. The triangles that combine to form a square fold onto each other.

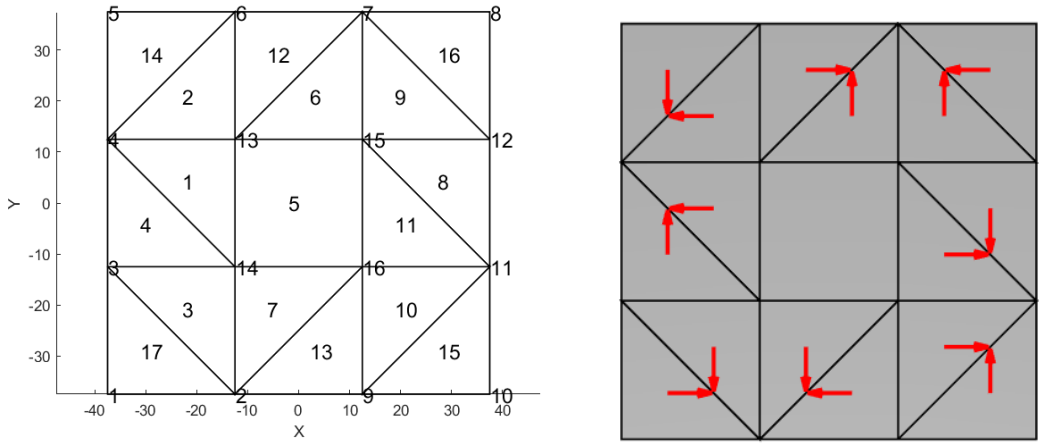

(a) (b)

Figure 33: (a) Huffman waterbomb origami pattern with the node and panel numbers. (b) Top view of the Huffman waterbomb origami pattern with red arrows to indicate the magnetic moment direction of the initial configuration.

The magnetic moment is defined for each panel the direction of which can be seen in Fig 33b. The directions of the magnetic moment are placed in such a way that if the origami is fully folded the magnetic moment would align with the direction of the magnetic field. For this example all magnetic moments would point towards the positive z direction. Since this pattern has 17 panels the magnetic moment matrix has 17 columns one for each panel:

$$M = 0.15 \cdot \begin{bmatrix} -1 & -1 & 0 & 0 & 0 & 0 & 0 & 0 & 0 & 1 & 1 & 1 & -1 & 0 & 0 & -1 & 1 \\ 0 & 0 & -1 & 1 & 0 & 1 & -1 & -1 & 1 & 0 & 0 & 0 & 0 & -1 & 1 & 0 & 0 \\ 0 & 0 & 0 & 0 & 0 & 0 & 0 & 0 & 0 & 0 & 0 & 0 & 0 & 0 & 0 & 0 & 0 \end{bmatrix} \text{Am}^2. \tag{53}$$

All panels have the same magnetic moment value of 0.15Am^2. A magnetic field of 40 mT is applied in the negative z direction which results in the following torque matrix:

$$\boldsymbol{\tau} = \begin{bmatrix} 0 & 0 & 6 & -6 & 0 & -6 & 6 & 6 & -6 & 0 & 0 & 0 & 0 & 6 & -6 & 0 & 0 \\ -6 & -6 & 0 & 0 & 0 & 0 & 0 & 0 & 0 & 6 & 6 & 6 & -6 & 0 & 0 & -6 & 6 \\ 0 & 0 & 0 & 0 & 0 & 0 & 0 & 0 & 0 & 0 & 0 & 0 & 0 & 0 & 0 & 0 & 0 \end{bmatrix} \text{Nmm}. \tag{54}$$

The torque generated from the magnetic actuation at the initial configuration is around the x and y axis. The resulting force decomposition consists of forces in the z axis. A summary of the simulation variables used for this example is shown below in table 7. The stiffness is the same as for the previous tests. The increment step is 0.25, this divides the applied field into 4 smaller increments. As a result $\boldsymbol{B}_a$ is increases by 10mT for each increment. Since for this example the deflection does not have to be accurate for each increment but only for the final increment a higher intermediate tolerance is used as described in the algorithm of section 3.3. The amount of panels is also a lot larger then for the previous tests so a larger final residual tolerance is used since the residual is larger for a higher amount of panels. For this test the panels also had to be less rigid for the solver in the MERLIN program to find a solution. This was done by lowering the stiffness of the bars, this allows the bars to stretch more easily and the panels to slightly deform. This is needed

since triangular panels unlike square panels aren't modeled with bending hinges that allow for the panel to deform.

Table 7: Variables used in the Huffman waterbomb simulation

$\boldsymbol{B}_a$(mT)	K_f(Nm/rad)	Damping	increment step	residual tolerance	intermediate tolerance
$\begin{bmatrix} 0 \\ 0 \\ -40 \end{bmatrix}$	0.1960	2	0.25	1	2

The final deflection that is obtained is shown in Fig. 34a. The model has the desired folding behavior that is expected for this pattern. The panels achieve a rotation of around 30° to 40°. The maximum deflection is at nodes 2,4,7 and 11 and is around 15.5mm.

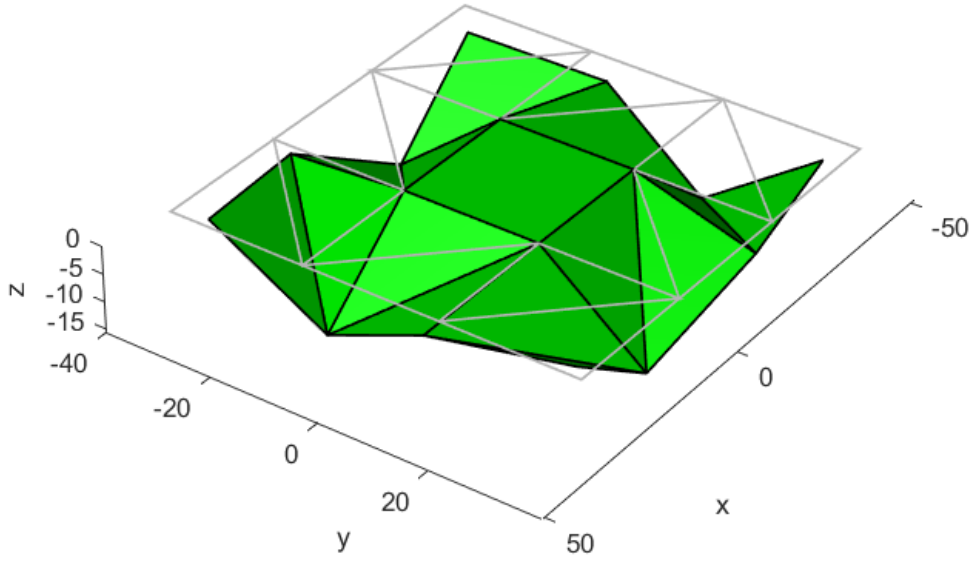

(a)

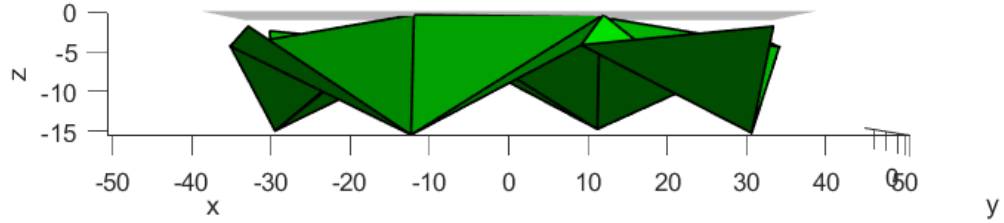

(b)

Figure 34: (a) The deflection of the Huffman waterbomb as a result of the applied magnetic field. (b) The side view of the deflected huffman waterbomb pattern.

5 Discussion

The magnetically actuated bar-and-hinge model had promising results with the samples tested in this paper. With the current model flat magnetic origami can be simulated in a uniform magnetic field. This could already be used to develop wireless deployable devices that fold and perform some operation based on an applied magnetic field.

There are however improvements and additions that can be made to the model. An important limitation is the application of the magnetic field since it is stationary during the folding of the origami. To achieve larger deformations the field could rotate as the panels are deforming. With a static magnetic field the panels rotate to align with the field but as the panels rotate the magnetic torque will decrease. If the magnetic field could rotate while it is deforming then larger deformation might be possible. This cannot be easily implemented into the current model since the deformation is always calculated from the unfolded state. If the applied field is rotated the forces applied on the structure are on the undeformed origami instead of on the already deformed origami. In order to achieve this an adaptive load needs to be applied to the structure that can change based on the change in magnetic field.

More additions to the magnetic actuation can be made. The model only considers a uniform field that generates a torque. However, if the field was not uniform, forces could also be generated and used to move the panels. The magnetic interaction between the magnets within the origami is also not included in the current model. Another limitation of the current model is the orientation of the origami in the initial configuration. The origami needs to start from a flat undeveloped state since that is the state in which the magnetic moments and the applied load are defined. However, origami structures are not always flat sheets but can have more complex shapes. To improve this the magnetic moments and load could be defined in the local coordinate system of each panel making it more general and allowing for many more origami structures to be tested.

The triangular and parallelogram panel shapes that currently work with the model already allow for a large variety of origami to be constructed. To have more possible panel shapes a force decomposition method would need to be found for that specific shape. A more general solution that works with different panel shapes could also be formulated. There is also a limitation with the parallelogram force decomposition. Since a parallelogram is skewed compared to a square the corners of the panel either move closer or further away from the center. The nodal force at the corners is obtained from the torque and the distance from the center. As a result, the nodes further away from the center have a small force and the point close to the center has a large force because the lever arm is different. This is not a problem for rigid panels since the panels do not bend much. However, if panel bending would be a larger factor then this needs to be taken into account.

When obtaining the simulation results for the examples shown in sections 4.4 and 4.5 some issues about the use of the MERLIN program occurred. The MERLIN program has settings that are used in the solver that solves the deformation, mostly related to the load factor in Eqn. 10. The settings are optimized for a load that is applied. However, since the magnetic load changes with each increment, the settings that work well for the first increment might not work for the last increment. In the examples, the settings were optimized for the last increment and inaccuracies of the intermediate steps were ignored. As an improvement to the model, the increment step size and amount of increments that are used with the load factor could be automatically adjusted as the magnetic load changes.

Another challenge with the MERLIN program is with triangular panels. The bending hinges used in parallelogram panels that allow the panels to bend are not present in triangular panels. So the triangular panels are more rigid with the same settings compared to square panels. In order to solve larger origami patterns it was found that panels that are fully rigid can have problems solving. A slight amount of panel bending would help in solving for the deformation, however, triangular panels cannot bend in the model. To compensate for this the bar stiffness was lowered instead, this allows for the three bars that make up the triangle to stretch. This will however result in the panels being stretched and deformed. Both issues with the MERLIN program could be resolved if the settings could be optimized based on the shape of the origami and the load applied to it. This currently has to be done manually and can affect the results or lead to no solution being found.

The two examples that were experimentally tested showed good results. The waterbomb pattern also showed the expected deformation and folding pattern that was simulated. The sample construction can still

be improved to be easier and more accurate. For the samples thin steel sheet was used that was manually cut to size, this can lead to errors which can be seen in Fig. 28 where the center hole is uneven. The panels are 3D printed and attached to the steel in the correct location using a 3D printed mold. When measured the dimensions have relatively large variance that could lead to less accurate results. Especially since the stiffness of the hinge is greatly effected by even small changes in the dimensions. Both of these production methods could be improved with, for instance, laser cutting of the hinges and panels.

One unexpected result obtained from the tests is the stiffness measurement. The stiffness was shown to be increasing while that is not modeled or expected. There could be a problem with the samples, for instance, the magnet is assumed to be rigidly attached to the panel while there could be some movement that is not taken into account. The measurement and calculation of the panel angles could also have issues that are unaccounted for. The position of the sample needs to be in the same direction as the applied field, this is also done manually and can lead to errors.

6 Conclusions and Future Work

The simulation framework developed in this report is able to simulate the deformation of complex magnetically actuated origami patterns. The method is able to simulate origami patterns with triangular and parallelogram panels which allows for a wide range of patterns to be simulated. From the experiments, it can be concluded that the deformation obtained in testing matches the simulated results. The testing methodology has some issues that could be improved. The calculated stiffness that is obtained from the tests showed unexpected results likely caused by some part of the experiment and the data analysis being inaccurate. For future testing more accurate construction and measurement of the samples would be needed. This allows for smaller origami to be constructed and tested. With this method, small-scale wireless devices can be simulated and designed. Such devices have potential applications in minimally invasive surgery.

In future work, the simulation framework can also be expanded. The current model considers only magnetic torque generated from a uniform magnetic field. If a non-uniform magnetic field is used, forces are generated on the magnet. If this is included in the model more options for magnetic actuation would be possible. The applied magnetic field is also assumed to be static. A changing magnetic field could lead to higher deflections and more complex magnetic control. This adaptation to the model likely requires large changes to the algorithm or a different method to be used.

References

[1] M Tonutti, DS Elson, GZ Yang, AW Darzi, and MH Sodergren. The role of technology in minimally invasive surgery: state of the art, recent developments and future directions. *Postgraduate Medical Journal*, pages 1–23, 2016.

[2] Lee Wilson, Sergio Pellegrino, and Rolf Danner. Origami sunshield concepts for space telescopes. In *Collection of Technical Papers - AIAA/ASME/ASCE/AHS/ASC Structures, Structural Dynamics and Materials Conference*, 2013.

[3] Evgueni T Filipov, Tomohiro Tachi, Glaucio H Paulino, and David A Weitz. Origami tubes assembled into stiff, yet reconfigurable structures and metamaterials. *Proceedings of the National Academy of Sciences of the United States of America*, 112(40):12321 – 12326, 2015.

[4] Sarah J. Wu, Hyunwoo Yuk, Jingjing Wu, Christoph S. Nabzdyk, and Xuanhe Zhao. A Multifunctional Origami Patch for Minimally Invasive Tissue Sealing. *Advanced Materials*, 33(11):2007667, 3 2021.

[5] Evin Gultepe, Sumitaka Yamanaka, Kate E Laflin, Sachin Kadam, Yoosun Shim, Alexandru V Olaru, Berkeley Limketkai, Mouen A Khashab, Anthony N Kalloo, David H Gracias, and Florin M Selaru. Biologic Tissue Sampling With Untethered Microgrippers. *Gastroenterology in Motion*, 144(4):691–693, 2013.

[6] Qiji Ze, Shuai Wu, Jun Nishikawa, Jize Dai, Yue Sun, Sophie Leanza, Cole Zemelka, Larissa S Novelino, Glaucio H Paulino, and Ruike Renee Zhao. Soft robotic origami crawler. *Science Advances*, 8(13), 2022.

[7] Chaoyu Cui, Xianmin Zhang, Benliang Zhu, Hai Li, Hongchuan Zhang, Rixin Wang, Jianhao Lai, and Ke Feng. A novel analysis method for magnetically actuated soft origami mechanisms. *Mechanism and Machine Theory*, 186(February):105353, 2023.

[8] Munkyun Lee and Tomohiro Tachi. Design and Evaluation of Compliant Hinges for Deployable Thick Origami Structures. *Proceedings of the IASS Annual Symposium 2023*, (July):10–14, 2023.

[9] Robert J. Lang, Kyler A. Tolman, Erica B. Crampton, Spencer P. Magleby, and Larry L. Howell. A Review of Thickness-Accommodation Techniques in Origami-Inspired Engineering. *Applied Mechanics Reviews*, 70(1):1–20, 2018.

[10] K. Liu and G. H. Paulino. Nonlinear mechanics of non-rigid origami: An efficient computational approach. *Proceedings of the Royal Society A: Mathematical, Physical and Engineering Sciences*, 473(2206), 2017.

[11] Edwin A. Peraza Hernandez, Darren J Hartl, and Dimitris C. Lagoudas. Active Origami. *Springer Nature*, 2019.

[12] Byoungkwon An, Nadia Benbernou, Erik Demaine, and Daniela Rus. Planning to Fold Multiple Objects from a Single Self-Folding Sheet. *Robotica*, 29:87–102, 2011.

[13] Ying Liu, Julie K Boyles, Jan Genzer, and Michael D Dickey. Self-folding of polymer sheets using local light absorption. *Soft Matter*, 8(6):1764–1769, 2012.

[14] Kjmagnetics. Magnet Grades, accessed 15-Jan-2024, https://www.kjmagnetics.com/blog.asp?p=magnet-grade, 2016.

[15] Geek3. Helmholtz Coil,Wikipedia, accessed 15-Jan-2024, https://en.wikipedia.org/wiki/Helmholtz_coil.

[16] Suyi Li, Hongbin Fang, Sahand Sadeghi, Priyanka Bhovad, and Kon Well Wang. Architected Origami Materials: How Folding Creates Sophisticated Mechanical Properties. *Advanced Materials*, 31(5):1–18, 2019.

[17] Mark Schenk and Simon Guest. Origami Folding: A Structural Engineering Approach. In *Proceedings of the 5th International Conference on Origami in Science, Mathematics and Education 5th International Conference on Origami in Science, Mathematics and Education*, 7 2010.

[18] E. T. Filipov, K. Liu, T. Tachi, M. Schenk, and G. H. Paulino. Bar and hinge models for scalable analysis of origami. *International Journal of Solids and Structures*, 124:26–45, 10 2017.

[19] Ke Liu and Glaucio H Paulino. Highly efficient nonlinear structural analysis of origami assemblages using the MERLIN2 software. *Origami*, 7:1167–1182, 2018.

[20] Tomohiro Tachi. Freeform Origami, accessed 15-may-2023,www.tsg.ne.jp/TT/software/, 2020.

[21] Hoffman-group. Feeler gauge catalog, accessed 3-April 2024, https://ecatalog.hoffmann-group.com/index.html?country=nld_NL_NLE/catalogs/&catalog=90000002#page_222, 2023.

[22] Kinovea. Kinovea-0.9.5, accessed 3-April-2024, https://www.kinovea.org/download.html, 2021.

A Appendix

A.1 AI declaration

During the preparation of this work the author used Grammarly in order to correct grammar mistakes and improve the sentence structure. After using this tool/service, the author reviewed and edited the content as needed and takes full responsibility for the content of the work. No other artificial intelligence tools were used during the preparation of this work.

A.2 Short paper submission MARSS2024

A short paper that was submitted and accepted for the annual International Conference on Manipulation, Automation and Robotics at Small Scales(MARSS). See next page.

A Modeling Framework using Bar-and-Hinge Model for Small Scale Magnetic Origami Devices

Sam Tijhuis[1], Venkatasubramanian Kalpathy Venkiteswaran[1,2]

***Abstract*— This paper presents a method for analyzing small-scale magnetically-actuated shape-changing devices using conventional origami kinematics. The primary contributions are formulations to decompose the magnetic load for analysis, and implementation of an iterative solver to calculate deformation under nonlinear force-deflection behaviour. The modeling framework is demonstrated using two simulations and validated through experiments on a magnetically-actuated waterbomb origami.**

I. Introduction

Origami engineering refers to the use of folding techniques from the art of origami to create foldable devices [1]. This method creates structures that can transform in ways that may not be possible with conventional engineering solutions. A reason to use origami in engineering is the shape changing ability of origami structures. Similar to when a flat piece of paper is folded to create various different origami shapes, engineering origami can create structures that have multiple resultant shapes depending on the folding process. Origami techniques have been used in large scales such as in aerospace engineering for deployable solar panels and sunshields [2] and for buildings and bridges [3]. At small scales, origami engineering also has been used in medical applications such as devices used in tissue sealing [4] or tissue biopsy [5].

A challenge with foldable origami is to actuate the folding movement. One way this can be achieved is with stimuli responsive materials like shape memory polymers [6]. Another way to generate the folding movement is by magnetic actuation, which allows for wireless control of these devices, particularly at small scales. With magnetic actuation, magnets are added to a device that can then be controlled by applying magnetic fields. The resultant loads steer the magnets and actuate the device [7]. Magnetically controlled origami have been used to create soft grippers that can be controlled wirelessly [8]. Eliminating the need for on-board batteries and other actuators also allows in making functional origami devices at small scales [9].

For designing origami devices it would be useful to have a method that is capable of simulating magnetically controlled origami structures. The use of magnets in origami allows for many different configurations of the magnets within the device to achieve a wide range of actuation responses. When small magnets are placed on individual panels of the origami structure, an externally generated magnetic field can be used to produce magnetic torques on the individual panels [10]. By optimizing the configuration of the individual magnets, it is possible to generate a (un)folding origami response to suit a given application. However, one of the primary challenges with magnetic origami is that the magnetic torque changes as the structure (un)folds, thus requiring an iterative solution for a theoretical model.

The work presented in this short paper uses a modified version of the bar and hinge model presented by Liu and Filipov [11] to approximate the mechanical behaviour of 3D origami structures under a uniform magnetic field . This model is able to simulate the deflection of an origami structure for any given crease pattern with predefined magnet placements and orientations. The study is validated through simulations of different shapes of magnetic origami. One of the structures is also experimentally demonstrated to undergo folding in a magnetic field (Fig. 1).

II. Theoretical Model

An example of magnetic actuation of an origami structure can be seen in Fig. 1. Each panel has a magnetic moment ($\boldsymbol{m}$), with directions indicated by arrows on each panel. An external uniform magnetic field ($\boldsymbol{B}$) creates a torque on the panels ($\boldsymbol{\tau} = \boldsymbol{m} \times \boldsymbol{B}$). The resultant magnetic torque tries to align each magnetic moment with the direction of the external field. The stiffness of the origami structure produces a counteracting effect, primarily caused by the stiffness of the origami hinges.

In this study, a bar and hinge model is used to calculate the deflection of origami structures under load [12]. The bar and hinge model is capable of calculating deflections as a result of forces applied to nodes in the structure. The magnetic actuation applies a moment to the center of a panel. For this reason a method to apply forces to the nodes based on a specified moment needs to be developed. The goal of this method is to obtain forces that result in the same deflection as applying a moment does. Two force decomposition methods were constructed; one for parallelogram panels and one for triangular panels. With these panel shapes a large variety of origami shapes can be constructed.

For a parallelogram panel, the force decomposition is performed in two steps. First, the applied torque ($\boldsymbol{\tau} = [\tau_x, \tau_y, \tau_z]$) is decomposed into four torques ($\boldsymbol{\tau}_i$) that are applied to each bar ($i = 1, 2, 3, 4$)of the parallelogram panel. Second, the decomposed torques are use to obtain the nodal force. The torque decomposition is shown in Fig. 2 with the applied torque shown in red and the four decomposed torques shown in black. For load equivalence,

[1]Surgical Robotics Laboratory, Department of Biomechanical Engineering, University of Twente, Enschede, The Netherlands.

[2]E-mail: v.kalpathyvenkiteswaran@utwente.nl.

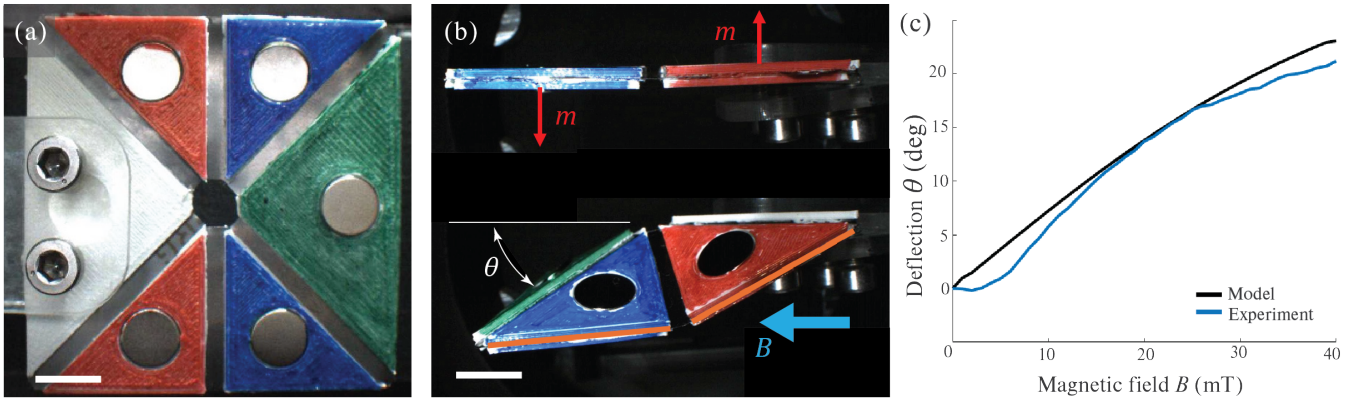

Fig. 1: (a) Waterbomb origami pattern with embedded magnets. Scale bar is 5mm. (b) Side view of origami deforming under magnetic field B, with magnetic moment m indicated by red arrows. (c) Comparison of deflection angle from theoretical model and experiment.

$$\boldsymbol{\tau}_1 = \boldsymbol{\tau}_3 = a_1 \boldsymbol{n}_1 + [0, 0, \frac{\tau_z}{4}] \tag{1}$$

$$\boldsymbol{\tau}_2 = \boldsymbol{\tau}_4 = a_2 \boldsymbol{n}_2 + [0, 0, \frac{\tau_z}{4}] \tag{2}$$

where

$$a_1 = \frac{\tau_y n_{2x} - n_{2y}\tau_x}{2n_{1y}n_{2x} - 2n_{1x}n_{2y}}, \tag{3}$$

$$a_2 = \frac{\tau_y n_{1x} - n_{1y}\tau_x}{2n_{2y}n_{1x} - 2n_{1y}n_{2x}}. \tag{4}$$

and $\boldsymbol{n}_i$ are normal vectors for each bar. From this, the nodal forces ($k = 1, 2, 3, 4$) can be calculated as

$$\boldsymbol{F}_k = \frac{1}{2}\frac{\boldsymbol{\tau}_p \times \boldsymbol{r}_p}{\boldsymbol{r}_p \cdot \boldsymbol{r}_p} + \frac{1}{2}\frac{\boldsymbol{\tau}_q \times \boldsymbol{r}_q}{\boldsymbol{r}_q \cdot \boldsymbol{r}_q} \tag{5}$$

where $\boldsymbol{r}_i$ are length vectors that go from the center of bars p and q which are adjacent to node k to their end points.

For a triangular panel the approach is similar to that of the parallelogram panel. The first step is create three outward normal torques that should add up to the applied torque. This can be seen in Fig. 2(b). However, in this case, the decomposition cannot be solved without adding more constraints. This issue can be overcome by using only two decomposed torques are necessary with the third one being zero.

As an example if $\boldsymbol{\tau}_2$ is chosen to be zero and the equations for the others torques are given as

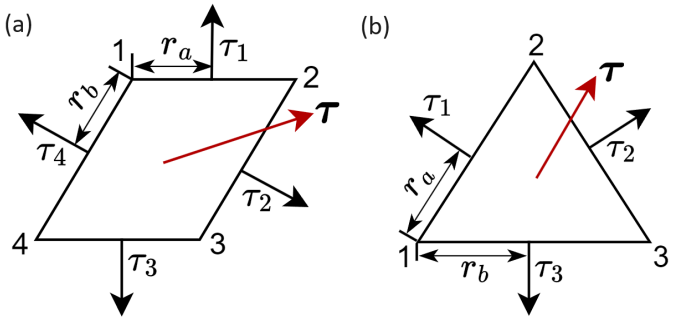

Fig. 2: Magnetic torque decomposition in (a) parallelogram and (b) triangular panels. a and b represent bars adjacent to node 1.

$$\boldsymbol{\tau}_1 = a_1 \boldsymbol{n}_1 + [0, 0, \frac{\tau_z}{3}] \tag{6}$$

$$\boldsymbol{\tau}_3 = a_3 \boldsymbol{n}_3 + [0, 0, \frac{\tau_z}{3}] \tag{7}$$

where the solutions to a_1 and a_3 are:

$$a_1 = \frac{\tau_x n_{3y} - n_{3x}\tau_y}{n_{1x}n_{3y} - n_{3x}n_{1y}}, \tag{8}$$

$$a_3 = \frac{\tau_x n_{1y} - n_{1x}\tau_y}{n_{3x}n_{1y} - n_{1x}n_{3y}}. \tag{9}$$

For different orientations and shapes of a triangular panel a different torque might be chosen to be zero giving similar equations for a_1, a_2 and a_3. Obtaining the nodal forces is done in the same way as for parallelogram panels.

To implement these formulations the MERLIN program developed by Liu et al. [13] is adapted to include magnetic actuation. An iterative process is implemented to account for the change in magnetic moment direction as the panels rotate (Algorithm 1).

Algorithm 1

Input : Damping and tolerances $damp$, tol
Initial magnet orientations $\boldsymbol{M}_0$
Output : Final magnet orientations $\boldsymbol{M}_1$
for $incr \leftarrow 0$ **to** 1 **do**
  $iter = 1$; $\boldsymbol{B}_{ai} = incr \cdot \boldsymbol{B}_a$
  while $res < tol$ **do**
    $\boldsymbol{\tau} = \boldsymbol{M}_{iter-1} \times \boldsymbol{B}_{ai}$ ▷ Magnetic torque
    $\boldsymbol{\tau} \rightarrow \boldsymbol{F}$ ▷ Nodal forces from torque
    $\boldsymbol{F} \rightarrow \boldsymbol{u}$ ▷ Calculate deflection (MERLIN)
    $\boldsymbol{u} \rightarrow \boldsymbol{M}_{iter}$ ▷ update $\boldsymbol{M}_{iter}$
    $\boldsymbol{M}_{iter} = \boldsymbol{M}_{iter-1} + (\boldsymbol{M}_{iter} - \boldsymbol{M}_{iter-1})/damp$
      ▷ Damping applied
    $iter = iter + 1$
    $res = norm(\boldsymbol{M}_{iter} - \boldsymbol{M}_{iter-1})$
      ▷ Residual is change in $\boldsymbol{M}_{iter}$
  end
  $\boldsymbol{M}_1 = \boldsymbol{M}_{iter}$
end

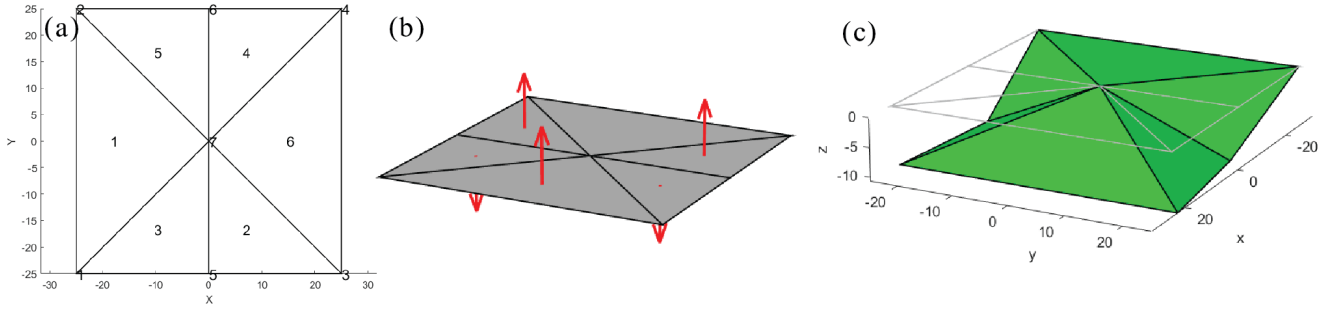

Fig. 3: (a) Waterbomb pattern panels and nodes (b) Magnetic moment directions (c) Deflected origami under X-direction magnetic field.

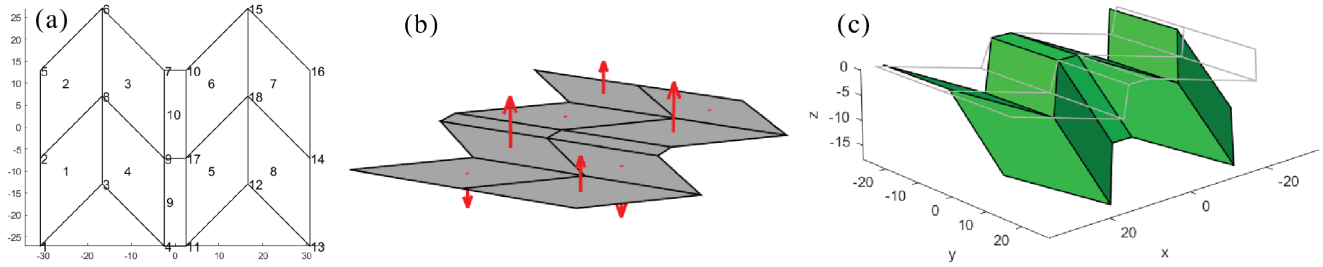

Fig. 4: (a) Adapted Miura-ori panels and nodes (b) Magnetic moment directions (c) Deflected origami under X-direction magnetic field.

III. Results

The solution process is tested in simulation of two origami patterns and experimental evaluation of one pattern. Simulations are carried out on a waterbomb pattern consisting of triangular panels and a miura-ori pattern consisting of parallelograms (Figs. 3 and 4).

The waterbomb pattern was also produced using a combination of 3D printing and sheet metal (Fig. 1). Magnets were added to the panels and the sample was subjected to an external magnetic field in a setup of electromagnetic coils. It is observed that the deflection angle matches the results from the theoretical model.

IV. Conclusions and Future Work

The methodology developed here allows for simulation of magnetically-actuated origami devices with complex magnetic orientations and for large deformations. The triangular and parallelogram panels cover a wide range of origami shapes. Currently, there are two major assumptions in this method: (1) the applied magnetic field is uniform and therefore only results in torques on the panels, and (2) the direction of the applied magnetic field does not change during actuation. Both of these can be addressed in future implementations.

This method can be used to design new origami-based deployable devices at small scales. It is envisioned that this approach will find use in the development of small-scale wireless devices, such as shape-morphing robots or therapeutic patches for minimally invasive surgical devices.

References

[1] R. J. Lang, K. A. Tolman, E. B. Crampton, S. P. Magleby, and L. L. Howell, "A Review of Thickness-Accommodation Techniques in Origami-Inspired Engineering," *Applied Mechanics Reviews*, vol. 70, no. 1, pp. 1–20, 2018.

[2] L. Wilson, S. Pellegrino, and R. Danner, "Origami sunshield concepts for space telescopes," in *Collection of Technical Papers - AIAA/ASME/ASCE/AHS/ASC Structures, Structural Dynamics and Materials Conference*, 2013.

[3] E. T. Filipov, T. Tachi, G. H. Paulino, and D. A. Weitz, "Origami tubes assembled into stiff, yet reconfigurable structures and metamaterials," *Proceedings of the National Academy of Sciences of the United States of America*, vol. 112, no. 40, p. 12321 – 12326, 2015.

[4] S. J. Wu, H. Yuk, J. Wu, C. S. Nabzdyk, and X. Zhao, "A Multifunctional Origami Patch for Minimally Invasive Tissue Sealing," *Advanced Materials*, vol. 33, no. 11, p. 2007667, 3 2021.

[5] E. Gultepe, S. Yamanaka, K. E. Laflin, S. Kadam, Y. Shim, A. V. Olaru, B. Limketkai, M. A. Khashab, A. N. Kalloo, D. H. Gracias, and F. M. Selaru, "Biologic Tissue Sampling With Untethered Microgrippers," *Gastroenterology in Motion*, vol. 144, no. 4, pp. 691–693, 2013. [Online]. Available: http://dx.doi.org/10.1053/j.gastro.2013.01.066

[6] M. T. Tolley, S. M. Felton, S. Miyashita, D. Aukes, D. Rus, and R. J. Wood, "Self-folding origami: Shape memory composites activated by uniform heating," *Smart Materials and Structures*, vol. 23, no. 9, pp. 0–9, 2014.

[7] Q. Ze, S. Wu, J. Nishikawa, J. Dai, Y. Sun, S. Leanza, C. Zemelka, L. S. Novelino, G. H. Paulino, and R. R. Zhao, "Soft robotic origami crawler," *Science Advances*, vol. 8, no. 13, 2022.

[8] C. Cui, X. Zhang, B. Zhu, H. Li, H. Zhang, R. Wang, J. Lai, and K. Feng, "A novel analysis method for magnetically actuated soft origami mechanisms," *Mechanism and Machine Theory*, vol. 186, no. February, p. 105353, 2023.

[9] V. K. Venkiteswaran, D. K. Tan, and S. Misra, "Tandem actuation of legged locomotion and grasping manipulation in soft robots using magnetic fields," *Extreme Mechanics Letters*, vol. 41, p. 101023, 2020.

[10] J. J. Abbott, E. Diller, and A. J. Petruska, "Magnetic methods in robotics," *Annual Review of Control, Robotics, and Autonomous Systems*, vol. 3, pp. 57–90, 2020.

[11] K. Liu and G. H. Paulino, "Nonlinear mechanics of non-rigid origami: An efficient computational approach," *Proceedings of the Royal Society A: Mathematical, Physical and Engineering Sciences*, vol. 473, no. 2206, 2017.

[12] E. T. Filipov, K. Liu, T. Tachi, M. Schenk, and G. H. Paulino, "Bar and hinge models for scalable analysis of origami," *International Journal of Solids and Structures*, vol. 124, pp. 26–45, 10 2017.

[13] K. Liu and G. H. Paulino, "Highly efficient nonlinear structural analysis of origami assemblages using the MERLIN2 software," *Origami*, vol. 7, pp. 1167–1182, 2018.